Journal of Petrology, 2026, **67**(10), egag092
https://doi.org/10.1093/petrology/egag092
Published: 13 OCTOBER 2026
Original Manuscript

OXFORD

Melting of a Lawsonite Eclogite Xenolith in the Colorado Plateau: Micropetrological Constraints on the Oligocene Thermal Pulse

RYO FUKUSHIMA [1,2,*], TATSUKI TSUJIMORI [2], NOBUYOSHI MIYAJIMA [3], SAYAKO INOUÉ [4], TIZIANA BOFFA-BALLARAN [3], GIACOMO CRINITI [3,5]

[1]Kochi Institute for Core Sample Research (EMS), Japan Agency for Marine-Earth Science and Technology , Monobe-otsu 200, Nankoku 783-8502, Japan
[2]Graduate School of Science, Tohoku University, Aramaki-aza-aoba 6-3, Aoba, Sendai 980-8578, Japan
[3]Bayerisches Geoinstitut, Universität Bayreuth, Universitätsstraße 30, 95440 Bayreuth, Germany
[4]Geodynamics Research Center, PIAS, Ehime University, Bunkyo-cho 2-5, Matsuyama 790-8577, Japan
[5]Department für Geo- und Umweltwissenschaften, Ludwig-Maximilians-Universität München, Theresienstraße 41, 80333 Munich, Germany

*Corresponding author. E-mail: ryofuku@jamstec.go.jp
Handling Editor: Prof. Joerg Hermann

The Navajo Volcanic Field in the Colorado Plateau (southwestern USA) is the only locality in the world where slab-derived high-pressure metamorphic rocks have been rapidly brought to the surface as xenoliths. As those xenoliths occur within serpentinized ultramafic microbreccias, they are interpreted to have been transported by an enormous explosion of the hydrated lithospheric mantle, rather than directly by deep-sourced magma. However, some xenoliths preserve evidence of a thermal pulse related to Oligocene Farallon slab tearing. Here, we examine records of the Oligocene thermal pulse in a lawsonite (pseudomorph)-eclogite xenolith with petrological characterization and crystallographic analysis. Garnet porphyroblasts in the xenolith record metasomatic overprinting by Mg-rich domains, and garnet cores were replaced by omphacite. These features suggest eclogite-facies metasomatism similar to those proposed in previous studies. However, omphacite has cation-disordered structure, and quenched felsic melt pockets of trondhjemitic to granitic composition are found as an array in omphacite, indicating that the xenolith was heated above 800 °C after eclogite formation. Lawsonite pseudomorphs are basically composed of euhedral zoisite, euhedral mica ($\sim pg_{50}\ marg_{50}$), anhedral to subhedral plagioclase ($\sim ab_{75}\ an_{25}$), and altered silicate glass. Omphacite grains enclosed in lawsonite pseudomorphs have zoisite-free halos in which peritectic aspidolite preferentially occurs. These observations suggest the past presence of hydrous silicate melt in lawsonite pseudomorphs and its crystallization at sufficiently low-*P* conditions at which plagioclase is stable. Multicomponent diffusion modeling of the metasomatized garnet constrains a short heating timescale to $<10^4$ years, but probably <10 years if directly interacted with a deep-sourced magma. Taken together, we argue that a transient magmatic episode first transported the eclogitized slab fragments into a shallower level (<60 km) in the subcontinental lithospheric mantle or overlying crust, which caused rapid heating, local flux melting, dehydration melting of lawsonite, and quenching to subsolidus temperatures. The xenolith then experienced the final explosive emplacement either immediately or after some period of subsurface storage.

Keywords Colorado Plateau, lawsonite eclogite xenolith, melt inclusion, omphacite, transmission electron microscopy (TEM)

Introduction

The Navajo Volcanic Field in the Colorado Plateau, southwestern USA, has hitherto been known as the only locality on Earth where slab-derived high-pressure metamorphic rocks were rapidly brought to the surface as xenoliths. In several diatremes, metamorphosed slab fragments have been found as coesite-bearing lawsonite eclogite, together with a great variety of sedimentary, igneous, and metamorphic rocks (e.g. Watson & Morton, 1969; Helmstaedt & Doig, 1975; Helmstaedt & Schulze, 1988; Usui *et al.*, 2003). Petrological, geochemical, and geophysical studies have revealed that low-angle subduction of the Farallon plate beneath the Colorado Plateau during the Laramide orogeny was followed by slab tearing, sinking and invasion of hot asthenospheric material (e.g. Humphreys *et al.*, 2003; Usui *et al.*, 2003; Smith *et al.*, 2004; Smith, 2010; Hoover *et al.*, 2020). It is therefore important to investigate detailed pressure–temperature–time (*P*–*T*–*t*) histories from those xenolith samples for the general understanding of non-steady tectonic processes in the final stage of flat-slab subduction.

The failure of flat-slab subduction generally induces prominent mass transfer with kilometer-scale migrations of both aqueous fluid and magma. In particular, large-scale explosive silicic volcanism called 'ignimbrite flareup' has received particular attention because of its unique characteristics compared to typical near-trench arc volcanism (e.g. Coney, 1978; Johnson, 1991; Best *et al.*, 2016). In

RECEIVED NOVEMBER 7, 2025. **REVISED** OCTOBER 5, 2026. **ACCEPTED** OCTOBER 8, 2026
© The Author(s) 2026. Published by Oxford University Press. All rights reserved. For commercial re-use, please contact reprints@oup.com for reprints and translation rights for reprints. All other permissions can be obtained through our RightsLink service via the Permissions link on the article page on our site—for further information please contact journals.permissions@oup.com.

Downloaded from academic.oup.com/petrology/article/67/10/egag092/8913147 by guest on 30 October 2026

the western USA, such magmatism occurred at 38–23 Ma in the surroundings of the Colorado Plateau (e.g. Karlstrom *et al.*, 2022). In addition, the slab foundering could have led to significant slab dehydration, and the liberated aqueous fluid caused hydration of the hanging-wall lithospheric mantle (e.g. Schulze *et al.*, 2015; Hoover *et al.*, 2020).

The peculiarity of slab-derived xenoliths in the Colorado Plateau lies not only in their rare origin but also in their exhumation process. In the Navajo Volcanic Field, several diatremes of serpentinized ultramafic microbreccias (SUM; McGetchin & Silver, 1972) and potassic mafic–felsic minettes are exposed, whose emplacement ages are 32–19 Ma (Naeser, 1971; Helmstaedt & Doig, 1975; Roden *et al.*, 1979; Laughlin *et al.*, 1986; Smith *et al.*, 2004). Although the SUM, which host slab-derived eclogite xenoliths, were formerly called 'kimberlites', they prove not to be true kimberlites because their petrological and geochemical features lack any evidence that they were originally magma (e.g. McGetchin & Silver, 1972; Roden, 1981). Several studies argue that minette magma intrusion caused a thermal pulse to heat up the hydrated mantle, thereby triggering devolatilization for the explosion of gas–solid (SUM) mixtures, which brought various xenoliths up to the surface (Smith & Levy, 1976; Smith *et al.*, 2004; Hoover *et al.*, 2020). Nevertheless, it remains uncertain what kind of heating processes caused the explosion. Considering the physical condition for hydrofracturing, or positive volume change through the devolatilization reaction (Nishiyama, 1989), the explosion of antigorite serpentinite matrix should occur at lower pressure than ∼2 GPa (e.g. Ulmer & Trommsdorff, 1995); however, coesite-bearing slab fragments have been exhumed in this locality, which must have originated from significantly higher pressure conditions.

A major barrier to solving this riddle is scarce constraints on to what extent the xenoliths suffered from heating during exhumation. A detailed investigation of this point will help us understand the actual medium bringing the xenoliths from depths. The only potential constraint was provided by Smith (2010), who revealed evidence of a later-stage thermal pulse from ultramafic xenoliths. They estimated the heating to have lasted for less than 1700 years based on Mg–Fe interdiffusion modeling in a compositionally zoned olivine. As the zonation in the olivine is characterized by a Mg-rich rim formed by chlorite breakdown, the temperature of the thermal pulse must have exceeded 750 °C. However, the pressure conditions at which the ultramafic xenoliths were heated were poorly constrained, and evidence of such a pre-explosion heating has never been clearly described from other xenoliths with different lithologies. The inspection of heating records in lawsonite eclogite xenoliths, or Farallon slab fragments, is thus of importance to understand the detailed explosion mechanism on a lithospheric scale. Unraveling the origin and spatiotemporal characteristics of the heat source may further constrain the general dynamics with slab tearing, possibly accompanied by asthenospheric intrusion or hot plume invasion.

In this study, we focus on an eclogite xenolith with lawsonite pseudomorphs from the Colorado Plateau to explore the record of later-stage heating. We perform crystallographic and micro-to-nanoscale petrological analyses of the lawsonite eclogite xenolith. Despite many previous studies on the subduction history of the Farallon slab, the following two aspects of the xenolith remain unexplored. First, the crystallographic features of omphacite have never been discussed. The space group of omphacite and its microstructure formed by cation ordering have potential to constrain the *T*–*t* path and the recrystallization kinetics (e.g. Carpenter, 1982*b* ; Fukushima *et al.*, 2021, 2024). Second, the texture of lawsonite pseudomorphs, most of which are occupied by tiny fibrous zoisite crystals, has been described only qualitatively. It is also worth examining because it may be related to the rapid heating of the xenolith. These investigations provide novel constraints on the pre- or syn-explosion heating event, and serves as a unique case study that illustrates the transient processes.

Background

The Colorado Plateau is an elevated region in the southwestern interior of the USA. It comprises unmetamorphosed and undeformed Paleozoic to Cenozoic sedimentary rocks on Proterozoic basement (Condie, 1982). The Farallon plate was subducting as a flat slab beneath this plateau during the late Cretaceous and Paleogene (e.g. Atwater, 1970; Karlstrom *et al.*, 2022), and its dip flattening followed by prolonged low-angle subduction led to eastward migration of arc magmatism (e.g. Coney & Reynolds, 1977; Lipman, 1992). Afterwards, the low-angle subduction ceased with tearing of the slab rather than a simple slab roll-back (Humphreys, 1995). This scenario has been confirmed by two independent directions of the magmatic front propagation (e.g. Coney & Reynolds, 1977; Clark *et al.*, 1982; Armstrong & Ward, 1991) and by the presence of a fallen slab revealed by modern mantle tomographic imaging (Schmandt & Lin, 2014).

Lawsonite eclogite xenoliths have been reported from the SUM diatremes, and they were investigated in several studies. Typical eclogites in the Navajo area (metabasic eclogites or 'Navajo eclogites') have mineral assemblages of garnet, omphacite, rutile, altered lawsonite (or pseudomorphs), and several minor minerals such as phengite, zircon, and rare quartz and coesite (e.g. Watson & Morton, 1969; Helmstaedt *et al.*, 1972; Smith & Zientek, 1979; Helmstaedt & Schulze, 1988; Usui *et al.*, 2003). Some eclogitic xenoliths consist mainly of jadeitic pyroxene and are close to monomineralic jadeitite (Tsujimori & Harlow, 2012). Their petrological features as Group-C eclogite (cf. Coleman *et al.*, 1965; Tsujimori & Mattinson, 2021) imply their similarity to those of Franciscan oceanic eclogites (Helmstaedt & Doig, 1975). The constituent minerals of the eclogite are significantly enriched in ^{18}O relative to mantle-forming minerals (e.g. Smith *et al.*, 2004), demonstrating their origin to be fragments of the Farallon slab. Petrological and geochemical investigations suggest that the eclogite was formed by the prograde metamorphism of altered mid-ocean ridge basalt (Usui *et al.*, 2006, 2007). On the other hand, U–Pb geochronology revealed the presence of Proterozoic zircon (Smith *et al.*, 2004) as well as of minerals forming in the late Cretaceous–Paleogene (Usui *et al.*, 2003; Smith *et al.*, 2004; Pohlner *et al.*, 2025). The significantly old zircon indicates that the eclogite protolith can be the overriding continental lithosphere brought down by subduction erosion. Some recent xenolith-based studies in the Farallon subduction zone suggest inland transport of eroded materials (Chapman *et al.*, 2020; Smith, 2020). In any case, one can assume that both the oceanic crust and eroded continental crust experienced a similar prograde metamorphism with subduction. Phase equilibrium modeling of a phengite-bearing eclogite xenolith has constrained the peak *P*–*T* conditions of the prograde metamorphism to 3.7 GPa and 620 °C (Hernández-Uribe & Palin, 2019).

Recent studies of the lawsonite eclogite xenoliths and other types of xenoliths have focused on the hydration process around the base of the continental lithosphere. Schulze *et al.* (2015) proposed the presence of hydration event at ∼28 Ma based on Th-Pb dating on accessory monazite, and related this event to many previous observations of

Downloaded from academic.oup.com/petrology/article/67/10/egag092/8913147 by guest on 30 October 2026

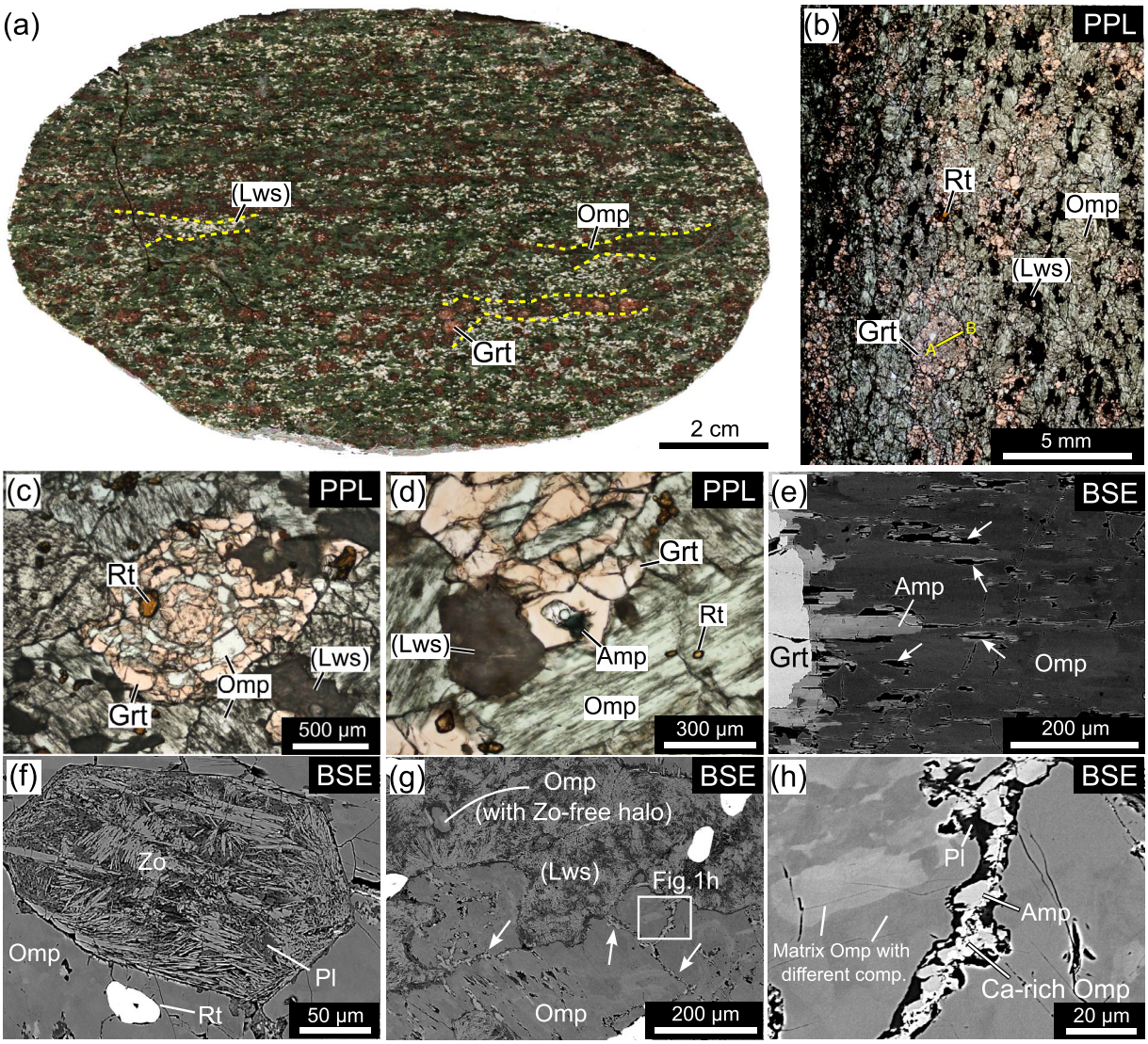


Figure 1 Photographs of the eclogite xenolith. (Lws) indicates lawsonite pseudomorphs. (a) Appearance of the polished xenolith sample. The yellow dashed lines highlight the morphology of mineral banding. (b) Plane-polarized (PPL) microphotograph of the analyzed thin section. The major-element compositional profile along the yellow line will be presented in Fig. 2c. (c, d) Enlarged PPL microphotographs. Matrix-forming omphacite grains tend to have a dusty appearance. (e) BSE image of the matrix-forming omphacite. The white arrows indicate dissolved pores. (f) BSE image of a lawsonite pseudomorph. The pseudomorph consists of micron-scale phases such as zoisite and plagioclase (see details in Fig. 4). (g) BSE image of another lawsonite pseudomorph. Omphacite enclosed in the pseudomorph is surrounded by a zoisite-free halo (see details in Fig. 5). The white arrows indicate veinlets extending from the pseudomorph, which crosscut matrix-forming omphacite. (h) BSE image of amphibole-rich veinlet adjacent to the lawsonite pseudomorph in (g). Compositional heterogeneity in matrix-forming omphacite is also presented.

hydrous minerals in mantle-derived xenoliths (e.g. McGetchin & Silver, 1970; Smith, 1995, 2010). They called this massive hydration event as 'Great hydration'. Hoover *et al.* (2020) investigated oxygen isotope zoning in garnet from the lawsonite eclogite xenoliths. They proposed that the metasomatic fluid originated from serpentine minerals in the sinking Farallon slab, and demonstrated a temporal link between the Great hydration event and the SUM dike formation. Several studies on halogen contents, and oxygen, hydrogen, and chlorine isotopes of mantle xenoliths supported that the metasomatic fluid came from the Farallon slab (Marshall *et al.*, 2017; Segee-Wright *et al.*, 2023, 2024). A few reports of garnetite xenoliths and discrete garnet crystals also suggest the presence of mantle metasomatism (Smith & Griffin, 2005; Sakamaki *et al.*, 2016), although the reported samples include those probably coming from asthenosphere below the Farallon slab (Sakamaki *et al.*, 2016). More recently, petrochronology of eclogite and omphacitite xenoliths revealed the presence of eclogite-facies metasomatism by Na–Si rich fluids that have predated the serpentinite-derived fluid infiltration (Pohlner *et al.*, 2025). Sr–Nd–S–O isotopic compositions of pyrite-bearing eclogite and omphacitite xenoliths corroborated that the Na–Si rich fluids, probably also enriched in S, were derived from siliceous metasediments (Aulbach *et al.*, 2026).

Methods

Sample preparation

We used an eclogite xenolith sample (~20 cm in size; Fig. 1a) collected from Garnet Ridge, central part of the Navajo Volcanic Field (sample

Downloaded from academic.oup.com/petrology/article/67/10/egag092/8913147 by guest on 30 October 2026

name: CLR-GR-O2T; courtesy of Dr Yoshihide Ogasawara, emeritus professor of Waseda University, Japan). The appearance of this xenolith sample has been reported previously (Tsujimori & Mattinson, 2021). From relatively fresh parts of the xenolith sample, we prepared polished thin sections (~60 μm in thickness) for the characterization of the mineral assemblage, rock texture, and mineral compositions. For single-crystal X-ray diffraction experiments, omphacite crystals were separated from the ~120–200 μm fraction (150–100 mesh) of the crushed xenolith sample by using a Franz magnetic separator at Tohoku University.

Mineral identification and electron microprobe analysis

The polished thin sections were analyzed by using a JEOL JSM-7001F field emission-scanning electron microscope (SEM) equipped with an Oxford INCA X-act energy dispersive X-ray (EDS) spectrometers at Tohoku University. All analyses described in this subsection were performed at a 15 kV acceleration voltage. The back-scattered electron (BSE) imaging and mineral identification were performed with a beam current of 1.4 nA, whereas the X-ray intensity maps of the lawsonite pseudomorphs were acquired with a beam current of 3.0 nA. EDS data and obtained map data were processed with the AZtec software (Oxford Instruments). Semi-quantitative analyses (using factory standards) were performed to evaluate major-element compositions of representative phases. Processed map data with the TruMap mode were re-processed to classify mineral phases by using the ImageJ software (Abràmoff *et al.*, 2004).

We collected a qualitative, thin-section scale X-ray intensity map in wavelength-dispersive (Ca, Mg, Mn, Na, Fe) and EDS (Al, Si, P, S, K, Ti, Cu) modes by using a JEOL JXA-iHP200F field-emission electron probe microanalyzer (EPMA) at Tohoku University. The mapping was performed with a beam current of 300 nA and a dwell time of 25 ms. In addition, the quantitative compositional analysis of the minerals (garnet, omphacite and zoisite) was performed by using a JEOL JXA-8200 EPMA at Bayerisches Geoinstitut (BGI) with a beam current of 10 nA and a spot size of 5 μm. This EPMA was also used for collecting X-ray intensity maps of a representative garnet porphyroblast. The maps (Mg, Al, Ca, Fe, Mn) were acquired with a beam current of 100 nA and a dwell time of 18 ms.

Post-hoc analysis of X-ray maps

All the X-ray intensity maps obtained with EPMA were processed and converted into phase maps with the software XMapTools 4.4 (Lanari *et al.*, 2014, 2019; Lanari & Tedeschi, 2025). For the representative garnet porphyroblast, a quantitative compositional map was additionally generated by calibrating the obtained X-ray intensity maps with the quantitative line profile.

The quantitative compositional map was further used for evaluating annealing timescale by diffusion modeling. Two representative diffusion profiles (DP-1 and DP-2) were carefully chosen and extracted from the map, and one-dimensional multicomponent (almandine, pyrope, grossular, spessartine) diffusion modeling was performed by using the software DIFFUSUP v1.13 (Chen *et al.*, 2024). The almandine component, which is most abundant in the investigated garnet, was regarded as a dependent component. Diffusion coefficients of the divalent cations in garnet were taken from Carlson (2006), and the effect of oxygen fugacity variation was ignored for simplicity (i.e. graphite–oxygen buffer is assumed), similarly as in a previous diffusion modeling (Hoover *et al.*, 2020). The initial compositional profile was set as a step function presumably generated by metasomatic replacement (e.g. Putnis, 2009; Martin *et al.*, 2011). The boundary concentrations were estimated by averaging five data points from each side. For the grossular profile, a small offset value (−0.005) was added to one end for better fitting. The initial step coordinate was approximated by the Matano interface for the pyrope profile. Although this coordinate would not be strictly identical to the initial step coordinate if cation diffusivity is spatially heterogeneous, we here ignored the difference for simplicity. The best-fit diffusion timescale and its uncertainty (derived from analytical uncertainties) were estimated as the posterior mean and standard deviation based on the Bayesian framework implemented in the software.

X-ray single crystal diffraction of omphacite

X-ray diffraction data of three representative omphacite crystals (CLR01, CLR02, CLR03) were collected by using an Oxford Diffraction Xcalibur 2 diffractometer at BGI. The system included a charge-coupled device (CCD) detector and graphite-monochromatized Mo-Ka radiation operated at 50 kV and 40 mA. 2D diffraction images were collected up to 2θ max. = 72°, with an exposure time of 60 s and steps of 0.5°. The measurement time was ~21 h per sample. Peak positions and intensities were extracted from the diffraction images using the CrysAlisPro software (Rigaku Oxford Diffraction), which was also employed to apply Lorentz, polarization, and numerical absorption corrections. The structure of each sample was solved and refined using the SHELX software package (Sheldrick, 2015) in the ShelXle graphical user interface (Hübschle *et al.*, 2011). In each structural model, the site occupancies of the M2 (Na, Ca) and M1 (Mg, Fe, Al) cation sites were fixed according to the averaged results obtained from EPMA, whereas the atomic coordinates and anisotropic displacement parameters of all atoms were refined against the squared structure factors F^2. Further details regarding the refinements can be found in the deposited crystallographic information files (CIFs).

TEM sample fabrication

The omphacite single crystals from which diffraction data were successfully obtained were mounted with epoxy resin and polished. A thin foil with a thickness of 100–150 nm was fabricated from each mounted grain using a focused ion beam (FIB) technique (Fig. S1). We used an FEI Scios DualBeam FIB-SEM system equipped with a gallium ion-gun and a thermal field emission electron gun at BGI, and the same FIB-SEM system at the Geodynamics Research Center at Ehime University (GRC). Representative compositions of the mounted grains were obtained by using the JXA-8200 EPMA at BGI under the same condition.

In addition to the mounted omphacite grains, omphacite located inside an atoll-shaped garnet grain (CLRTS_04) and three lawsonite pseudomorphs (CLR_ZoPs_01 and CLR_ZoPs_03: only pseudomorph; CLR_ZoPs_02: including an interface between omphacite and pseudomorph) were also fabricated directly from a thin section into thin foils by using the FIB technique.

TEM observation and nanoscale analysis

The thin foil specimens of omphacite were observed by using an FEI Titan G2 80-200 S/TEM system at BGI for textural observation,

Downloaded from academic.oup.com/petrology/article/67/10/egag092/8913147 by guest on 30 October 2026

compositional measurement, and compositional mapping. All analyses described in this subsection were performed at a 200 kV acceleration voltage. The degree of order of each omphacite specimen was evaluated by acquiring selected area electron diffraction (SAED) patterns along certain zone axes (e.g. *c*-axis). To reduce the effect of multiple scattering, beam precession was introduced for some SAED measurements. Bright-field (BF) and dark-field (DF) TEM images were also obtained. Representative major-element compositions were measured by selecting several regions of interest from EDS X-ray maps collected by scanning transmission electron microscopy (STEM). The EDS spectra data were processed by using the Esprit software (Bruker), with the Cliff-Lorimer method for Z-number correction (Cliff & Lorimer, 1975) and absorption correction (van Cappellen & Doukhan, 1994). As for details of the measurement and analytical methods, see Fukushima *et al.* (2024).

The thin foil specimens of lawsonite pseudomorph were observed by using the same system at BGI (for CLR_ZoPs_01 and CLR_ZoPs_02), and a JEOL JEM-2100F S/TEM (equipped with a silicon drift detector DrySD60GV) at GRC (for CLR_ZoPs_01 and CLR_ZoPs_03). SAED patterns of each phase, BF-TEM images, and EDS X-ray maps of representative areas were obtained for the characterization of lawsonite pseudomorph. The EDS spectra for the CLR_ZoPs_03 were obtained at GRC, and processed by using the Noran System 7 software (Thermo Fisher Scientific), with the correction based on experimentally calibrated k-factors and the assumed specimen thickness.

All the analyses of SAED patterns for the mineral identification were performed by using the ReciPro software (Seto & Ohtsuka, 2022).

Thermodynamic modeling and mass-balance calculation

The following calculation methods were applied to discuss the petrographic observations, especially local reaction textures. Thermodynamic calculations were performed by using the software THERMOCALC v3.51 (Powell *et al.*, 1998; Holland & Powell, 2011). The Reactions software (by Dmitry Dolivo-Dobrovolsky; http://www.dimadd.ru/en/Programs/reactions) was also used to confirm whether a discontinuous reaction among multiple minerals was algebraically allowed.

Sample petrography

In this section, we describe individual minerals in the xenolith based on SEM–EDS and EPMA analysis. Mineral abbreviations follow Warr (2021). The sample shows a compositional banding composed of alternating garnet-rich and -poor layers (Fig. 1a, b). The mineral assemblage and modal proportions are: omphacite (70.7%), garnet (16.7%), lawsonite pseudomorphs (zoisite-rich aggregates; 11.6%), and rutile (0.7%) (based on surface area proportions in the phase map shown in Fig. S2; map size = 2.4 × 1.5 cm^2). As accessory phases, plagioclase, chlorite, sodic-calcic amphibole, zircon, barite, and Fe–Ti oxide were identified with SEM–EDS point analyses. Neither phengite nor SiO_2 polymorph was found in our sample. Representative mineral compositions of garnet, omphacite, zoisite, amphibole, and other minor phases are presented in Tables S1–S7.

Omphacite

The matrix-forming omphacite grains are compositionally heterogeneous ($quad_{35–50}$ $jd_{30–50}$ $aeg_{10–25}$; Figs 1h and 2a, Tables S2 and S3), and characterized by the presence of elongated pores (10–20 μm in width; white arrows in Fig. 1e) and tiny pits (<5 μm in size). Their dusty appearance in the optical microscope (Fig. 1c, d) appears to be attributed to those micron-scale structures. The elongated pores are aligned in a specific direction within each grain, probably parallel to the c axis of omphacite. Notably, some omphacite grains enclosed in garnet lack such textures (Fig. 1c).

Garnet

Garnet occurs as porphyroblasts (typically 1–2.5 mm in size) with dense microcracks (Fig. 1c) filled by other minerals or healed by garnet itself. The major-element compositional profile of the largest garnet in the thin section ($alm_{58–62}$ $prp_{15–24}$ $grs_{15–20}$ $sps_{2–5}$ $adr_{0–4}$; Table S1) shows a rimward increase in Mg# = 100 × Mg/(Mg + Fe^{2+}) atomic ratio (Fig. 2c), which is consistent with previous reports of prograde garnet zoning (e.g. Usui *et al.*, 2006). However, X-ray maps of the garnet porphyroblast show that its major element compositions were modified along microcracks (Fig. 3b, c). This modification, which shifted the garnet compositions toward Mg-rich, and Ca- and Mn-poor direction, appears to have obliterated most of the original prograde zoning textures (Fig. 3c, d). The garnet compositions are thus grouped into two distinct generations with a threshold of $X_{prp} \sim 0.15$: Grt-1 (Mg-poor) and Grt-2 (Mg-rich) (Fig. 3d, e). In addition, the atoll-shaped feature with a preferential replacement of garnet core by omphacite (Fig. 3a) indicates post-metamorphic fluid infiltration and high-*P* metasomatism (Cheng *et al.*, 2007; Faryad *et al.*, 2010), as described in previous studies of Navajo eclogites (e.g. Hernández-Uribe & Palin, 2019; Pohlner *et al.*, 2025).

Lawsonite pseudomorphs

Lawsonite pseudomorphs are ubiquitously found in the xenolith sample, mainly in the matrix and occasionally as inclusions in garnet porphyroblasts (Fig. 3a). Pristine lawsonite, which was confirmed in previous studies (e.g. Usui *et al.*, 2006; Hernández-Uribe & Palin, 2019), was not found in our sample. Nonetheless, the polyhedral outline of the aggregate indicates the original shape of the lawsonite crystal (Fig. 1f). Some lawsonite pseudomorphs are accompanied by radial cracks into surrounding matrix minerals (Fig. S3). X-ray maps of the lawsonite pseudomorph reveal the presence of at least three phases other than zoisite (Fig. 4a). The modal proportions are: zoisite = 49.7%; Si-rich phase (plagioclase) = 12.7%; Mg-rich phyllosilicate = 11.7%; and Ca-poor, Al-rich phase (probably mica) = 26.0% (Fig. S4). In addition, omphacite enclosed in lawsonite pseudomorphs is selectively surrounded by a halo with zoisite-free phase assemblages (Figs 1g and 5a, b), composed of plagioclase and Mg-rich phase aggregates (Fig. 5c). Plagioclase tends to occur on the omphacite side (Fig. 5c), but it does not necessarily cover the whole surface of the omphacite grain (Fig. 5b). Detailed descriptions of the mineral assemblages are given in the later sections.

Amphibole and associated minerals

Sodic-calcic amphibole (magnesiotaramite) occurs along dissolved pits and microcracks in matrix-forming omphacite, in contact with garnet (Figs 1d, e and 3b, Table S5). In addition, arrays of sodic-calcic amphibole (barroisite) are present as veinlets extending from lawsonite pseudomorph, which crosscut matrix-forming omphacite (Fig. 1g, h, Table S5). These amphibole arrays are surrounded by albite (~ab_{90}

Downloaded from academic.oup.com/petrology/article/67/10/egag092/8913147 by guest on 30 October 2026

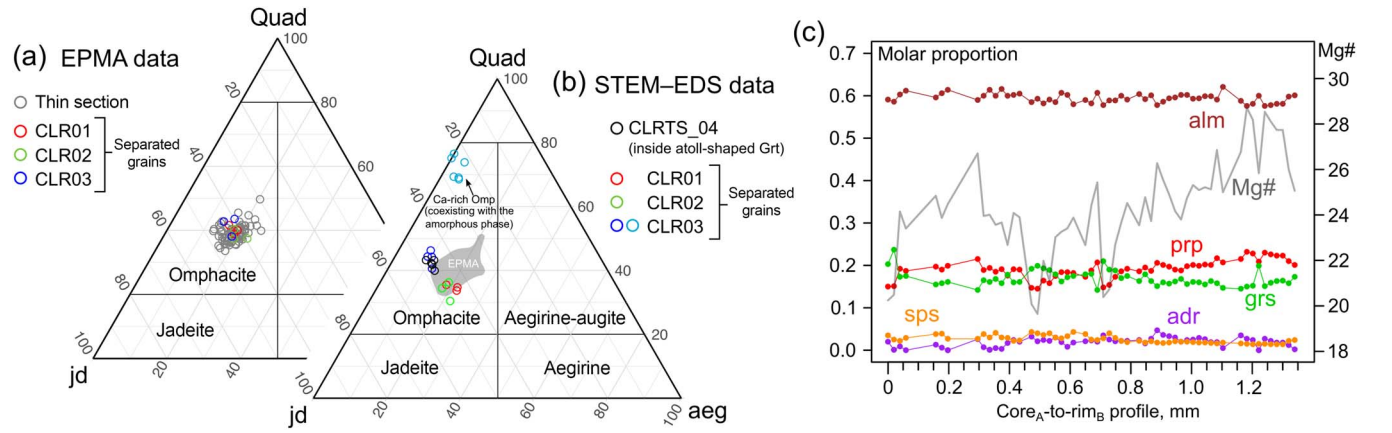


Figure 2 Major-element compositions of omphacite and garnet. (a) Compositional variation of omphacite (measured with EPMA). The data labeled as 'thin section' were obtained by spot analyses of matrix-forming omphacite with random sampling on a single thin section. (b) Compositional variation of omphacite (measured with STEM-EDS). The gray field indicates the range of EPMA data. Note that the light-blue circles represent the compositions of Ca-rich omphacite found in CLR03 (see details in Fig. 7). Nomenclature after Morimoto *et al.* (1988). (c) Core-to-rim line profile of the representative garnet porphyroblast in Fig. 1b.

$an_{10;}$ Table S6) and accompanied by Ca-rich omphacite (~$quad_{70}$ jd_{23} aeg_7; Table S7) (Fig. 1h). The interface between the plagioclase and matrix-forming omphacite is locally characterized by wavy morphology. Chlorite also occurs along microcracks cutting garnet and omphacite, locally together with amphibole (Fig. 3b).

Other minerals

Barite occurs both as thin veinlets in matrix-forming omphacite (Fig. S5a) and inclusion in garnet (Fig. S5b). Fe–Ti oxide locally occurs as a partial replacement of rutile.

Crystallographic features of omphacite

Cation ordering state in omphacite reflects thermal histories of eclogite. Omphacite found in low-*T* eclogite (i.e. Group-C eclogite) usually exhibits the *P2/n* space group (ordered structure) due to splitting of each cation sites (M1 and M2) into two separated sites (M1, M11 and M2, M21) (Matsumoto *et al.*, 1975), since their metamorphic peak temperatures do not exceed the critical temperature (~865 °C; Carpenter, 1982*a*) as long as the chemical composition is within a typical range (e.g. Carpenter, 1980; Müller *et al.*, 2011; Fukushima *et al.*, 2021, 2024). Annealed at higher temperature, cation disordering occurs to exhibit the *C2/c* space group (e.g. Fleet *et al.*, 1978; Boffa-Ballaran *et al.*, 1998).

Our X-ray diffraction measurements revealed that the diffracted intensities from the ordered phase (*P2/n*) were systematically extinct (below 3-sigma level) for all the three crystals. Therefore, the crystal structures were refined in the *C2/c* space group (Table 1). Our TEM observation of omphacites consistently demonstrated the absence of antiphase boundaries and of electron diffraction peaks from the ordered phase (i.e. 0k0 (k = odd)) in the SAED patterns acquired with beam precessions for all the crystals (Fig. 6c, Fig. S6). However, their SAED patterns acquired with no beam precessions show significantly weak and broad electron diffraction, or diffuse scattering, of 0k0 (k = odd) (Fig. 6a, b, Fig. S6). The difference in diffraction intensities with and without beam precession is due to the extent of multiple electron scattering (or 'double diffraction') in the specimens. Since the extinction of 0k0 (k = odd) diffraction peaks in omphacite is caused by the Bravais lattice change with cation disordering, the investigated omphacite would still retain slightly ordered structures, likely with short-range order.

Additional features revealed by FIB-TEM analysis

Nanoscale compositional analysis of omphacite

The major element compositions of omphacite obtained from the STEM–EDS analyses are presented in Tables S8 and S9. Based on the Fe^{3+} content estimation with $Fe^{3+} = Na - Al$ and endmember calculations (e.g. Fukushima *et al.*, 2024), the STEM–EDS data tend to overestimate the jadeite component compared to the EPMA results, whereas no systematic difference was found in the aegirine component between STEM–EDS and EPMA (Fig. 2b). According to the STEM–EDS results, CLR01 and CLR02 are more enriched in the aegirine content than CLR03 (Fig. 2b), but this trend is not clearly observed in the EPMA data (Fig. 2a).

Amorphous phase in omphacite

In the course of TEM observation of separated omphacite crystals, we unexpectedly found an array of micron-scale crystals and amorphous phases with void in one of the omphacite specimens (CLR03; Fig. 7a, b). Their occurrence is characterized by a string-of-beads texture locally connected to dislocations in the host omphacite (Fig. 7a, f). The largest clot bounded by the dislocations (which we call 'the polyphase pocket'; Fig. 7c–e) is composed of amorphous phase with trondhjemitic to granitic compositions (73–75 wt % SiO_2, 18–19 wt % Al_2O_3, <1 wt % CaO, 3–5 wt % Na_2O, and 3 wt % K_2O; Table 2), Ca-rich omphacite ($quad_{65–75}$ $jd_{20–30}$ $aeg_{0–5}$; Fig. 2b), and minor amounts of K-bearing phyllosilicates (Fig. 7e): muscovite (Si = 3.2 a.p.f.u. for O = 11) and wonesite (general formula: $(Na, K)_{0.5}(Mg, Fe, Al)_3(Si, Al)_4O_{10}(OH)_2$). Representative compositions of the minerals are presented in Table S10.

The amorphous phase has a flat, smooth appearance in BF-TEM and STEM-HAADF images (Fig. 7a, c, d). Its SAED pattern shows a diffuse ring with a spacing of approximately 3–4 Å (0.3–0.4 nm) (Fig. 7c). The Ca-rich omphacite occurs preferentially at the edge of the amorphous

Downloaded from academic.oup.com/petrology/article/67/10/egag092/8913147 by guest on 30 October 2026

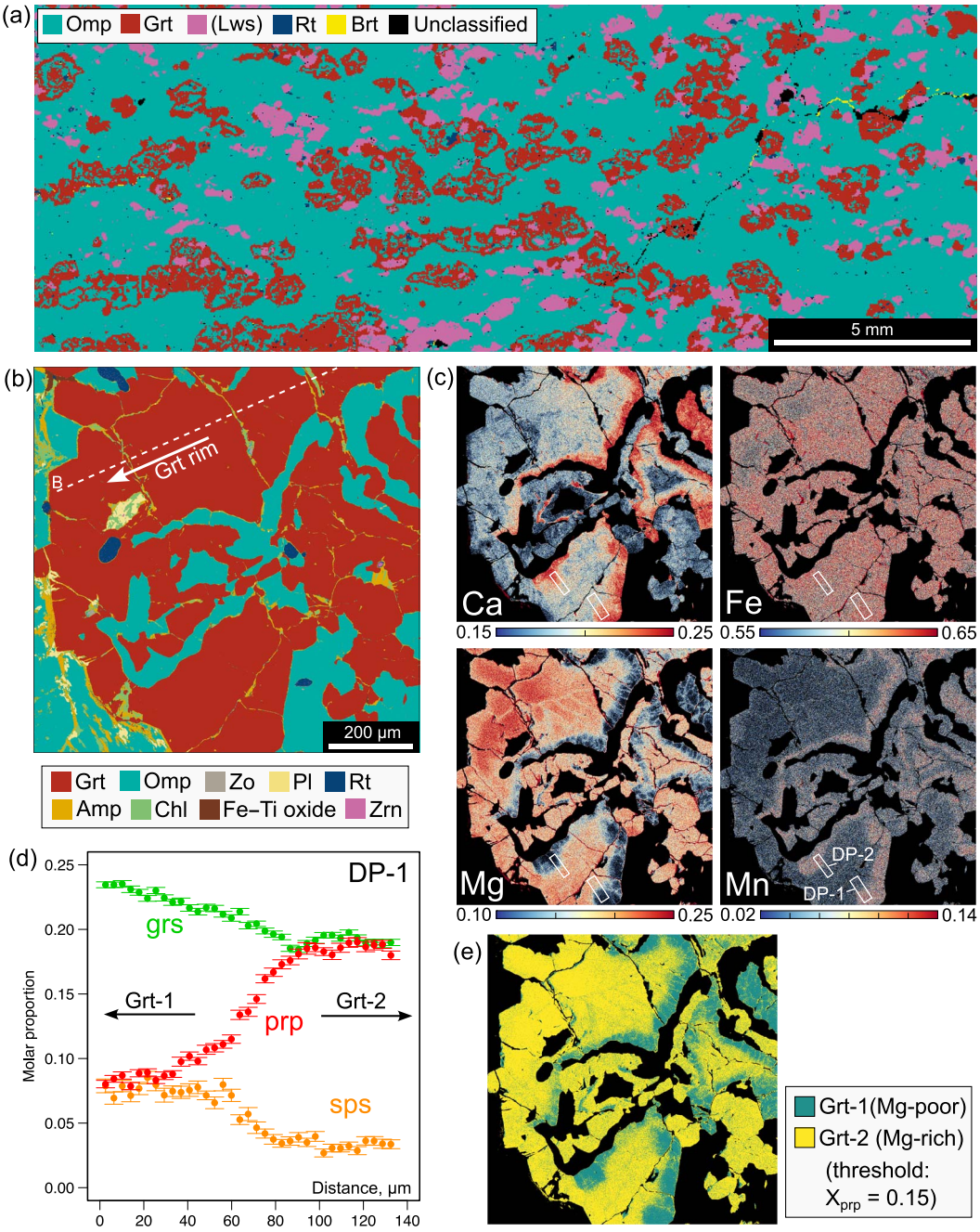


Figure 3 Spatial distribution of minerals and compositional heterogeneity in garnet. (a) Thin-section scale phase map generated from X-ray intensity maps. (b) Phase map around the representative garnet porphyroblast (same grain as shown in the lower part of Fig. 1b). (c) Quantitative compositional maps of the garnet (Ca, Fe, Mg, and Mn; a.p.f.u. in garnet with O = 4). (d) One of the compositional line profiles of garnet extracted from (c) (DP-1; prp, grs, and sps; error bar: ±1σ). (e) Spatial distribution of Mg-poor and Mg-rich garnet (Grt-1 and Grt-2).

phase (Fig. 7a, d, e) with abundant stacking defects on the (010) plane (Fig. 7c).

Phase assemblage of lawsonite pseudomorphs

Our FIB-TEM analysis revealed the presence of micron-scale crystals (zoisite, plagioclase, mica) and interstitial amorphous material (IAM) in lawsonite pseudomorphs (Fig. 4c–f). We also found aspidolite (~6 wt % Na_2O) rimmed by phlogopite and the albite (~ab_{90} an_{10})–alkali feldspar (~or_{90} ab_{10}) pair in the zoisite-free halo around an omphacite grain enclosed in a lawsonite pseudomorph (Fig. 5d–f). In addition, as submicron phases, fibrous Mg-rich phyllosilicates occur as aggregates with abundant intercrystalline porosity (Figs 4d and 5d–g). Representative mineral compositions measured with STEM–EDS are presented in Table S11.

Euhedral tabular zoisite is the dominant phase in the pseudomorph. The zoisite crystals have inner cores and overgrown Fe-rich rims (Fig. 4d, e). The mica crystals are almost K-free and Ca-rich (~pg_{50}

Downloaded from academic.oup.com/petrology/article/67/10/egag092/8913147 by guest on 30 October 2026

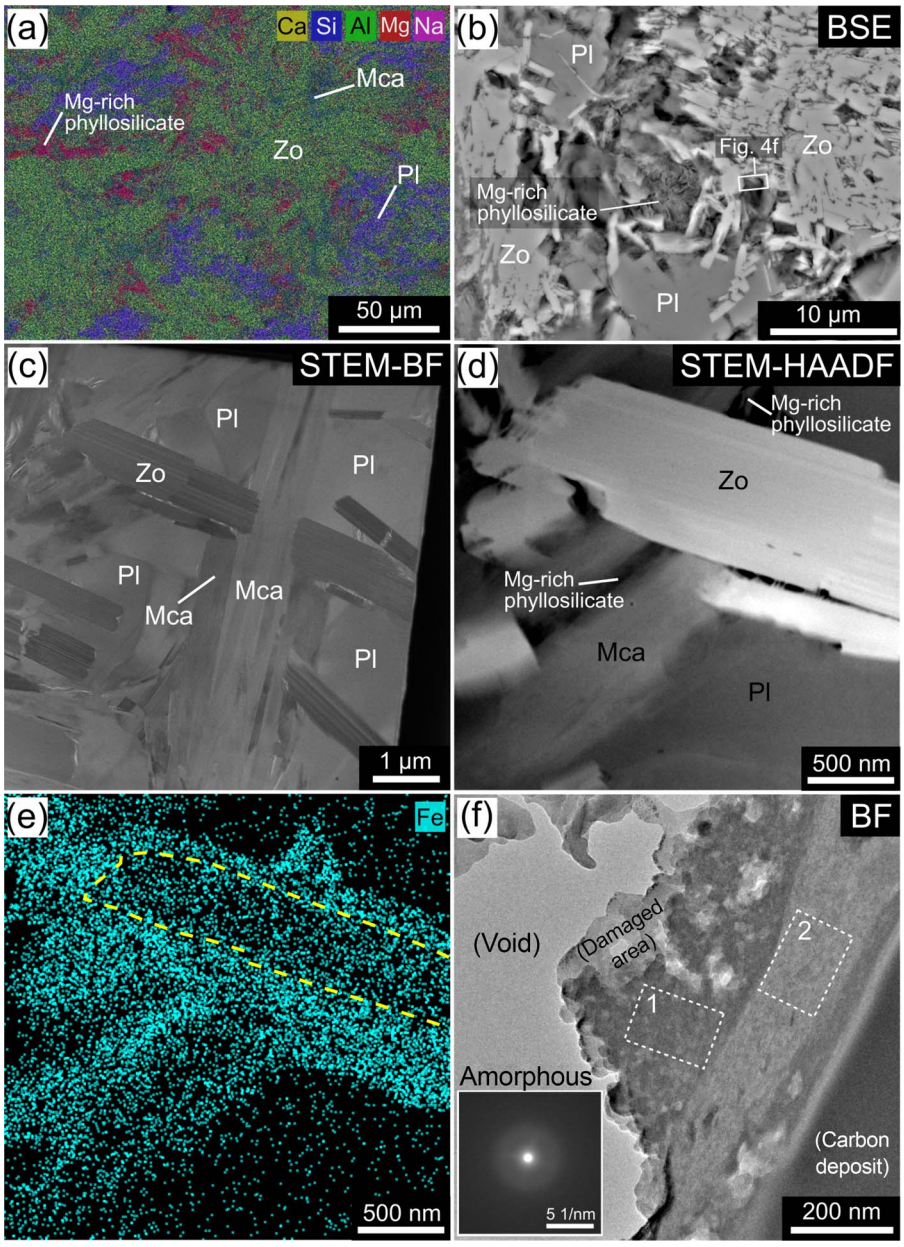


Figure 4 Summary of micropetrography of lawsonite pseudomorphs. (a) Combined X-ray intensity maps (Ca, Si, Al, Mg, Na). (b) Enlarged BSE image. (c) STEM-BF (bright field detector) image of a lawsonite pseudomorph (CLR_ZoPs_01). (d) STEM-HAADF (high-angle annular DF detector) image of the lawsonite pseudomorph (CLR_ZoPs_01). (e) X-ray intensity map (Fe) of the same region as (d). Zoisite has overgrown with an Fe-rich rim (bounded by the yellow dashed line). (f) BF-TEM image of IAM presented in (b) (CLR_ZoPs_03). The dashed squares 1 and 2 indicate the representative areas for the compositional analysis with STEM–EDS (dark and bright area, respectively). As an inset, the SAED pattern is presented.

$marg_{50}$) and occur as euhedral tabular crystals (Fig. 4c, d). By contrast, plagioclase (~ab_{75} an_{25}) occurs as anhedral to subhedral crystals (Fig. 4c, d).

Apart from the minerals described above, we found IAM in the lawsonite pseudomorph (Fig. 4b, f). BF-TEM imaging revealed its rough and uneven texture, apparently consisting of nanoparticle aggregates (10–30 nm in size) (Fig. 4f). A banding texture was found as a spatial heterogeneity in the BF contrast (Fig. 4f). The IAM occurs together with void and damaged area by Ga-ion beam (Fig. 4f). The spacing of the diffuse ring in the SAED pattern is ~3–4 Å. Its chemical composition (normalized without H_2O) is characterized by 57–60 wt % SiO_2, 14–16 wt % Al_2O_3, and 7–8 wt % CaO, but it also contains an unusually high amount of Fe (~8 wt % FeO), and Zn and S at the weight percent level (Table 2).

Aspidolite rimmed by phlogopite and the albite–alkali feldspar pair, which were found only in the zoisite-free halo, occur as euhedral crystals in a matrix composed of Mg-rich phyllosilicate (Fig. 5d–f). The Mg-rich phyllosilicate laths are typically characterized by significantly small widths (<150 nm) compared to other pseudomorph-forming euhedral minerals (zoisite and mica: 500–1000 nm), although a few grains adjacent to phlogopite have thicker, tabular morphologies (Fig. 5e, f). Chemical compositions of the Mg-rich phyllosilicate can be approximated by those of chlorite (enriched in Mg–Al–Si and total cations ~10 with O = 14, Si = 2.6–3.5 a.p.f.u.; Table S11 and Fig. S7),

Downloaded from academic.oup.com/petrology/article/67/10/egag092/8913147 by guest on 30 October 2026

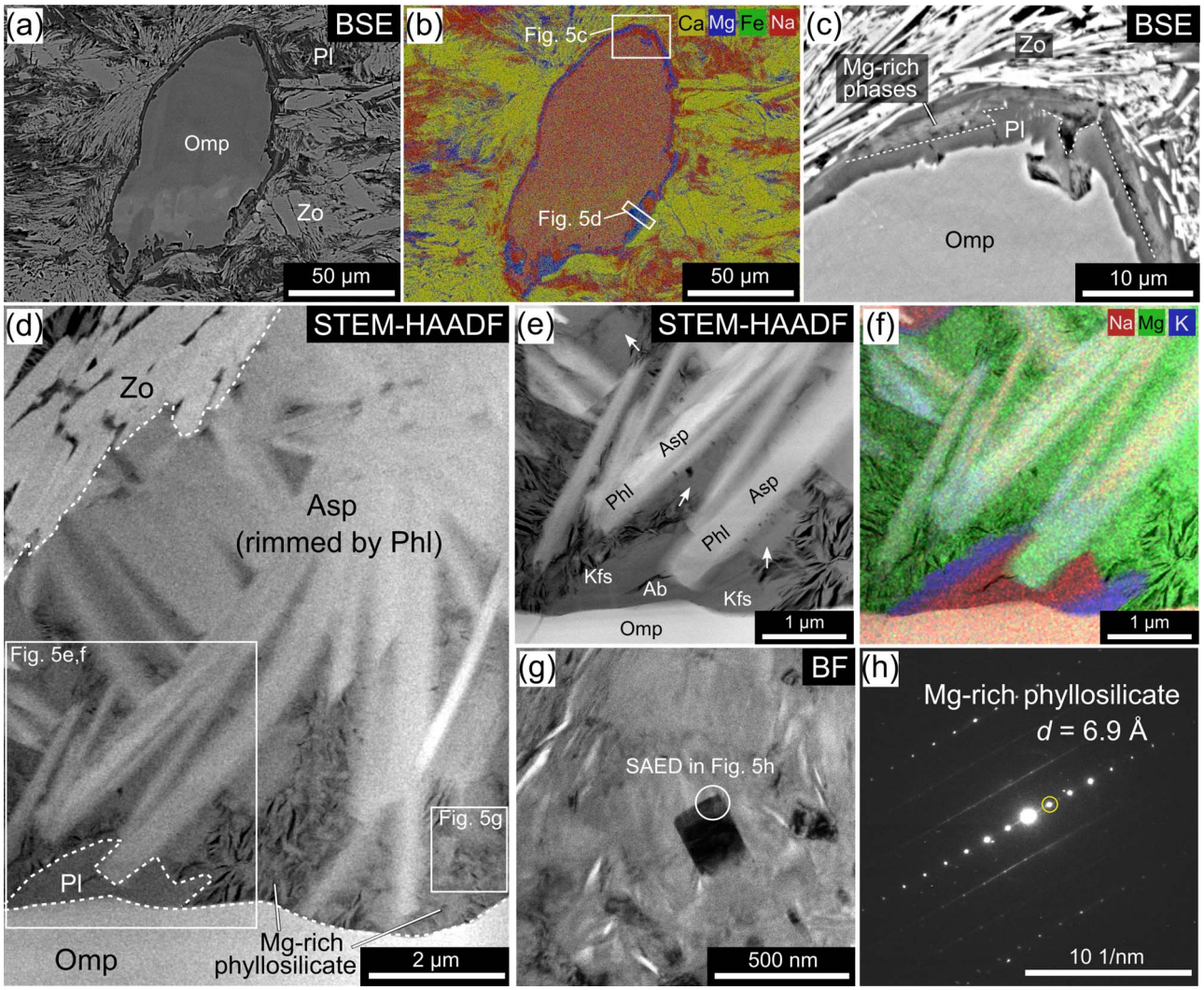


Figure 5 Zoisite-free halo found at the rim of omphacite enclosed in lawsonite pseudomorphs. (a) BSE image of omphacite enclosed in a lawsonite pseudomorph. (b) Combined X-ray intensity maps (Ca, Mg, Fe, Na) of the same region as (a). (c) Enlarged BSE image of the zoisite-free halo. (d, e) STEM-HAADF images of the zoisite-free halo (CLR_ZoPs_02). The white arrows in (e) indicate the thick-tabular type of Mg-rich phyllosilicate. (f) Combined X-ray intensity maps (Na, Mg, K) of the same region as (e). (g) BF-TEM image of the representative grain of Mg-rich phyllosilicate. (h) SAED pattern of the Mg-rich phyllosilicate (with 1.5° beam precession).

but its basal spacing is 6.9 Å (Fig. 5h), showing the crystal structure is different from that of typical chlorite with 14 Å spacing.

Discussion

Eclogite-facies metasomatism recorded in garnet and omphacite

The compositional modification along microcracks in garnet suggests metasomatism after the garnet nucleation and growth (Fig. 3). The significant increase in pyrope content from Grt-1 (~0.08) to Grt-2 (~0.18) is consistent with previously described features of later-stage eclogite-facies metasomatism, which was probably caused by serpentinite-derived fluids (Hoover *et al.*, 2020; Pohlner *et al.*, 2025). The compositional heterogeneity in matrix-forming omphacite (e.g. Fig. 1h) would also reflect eclogite-facies metasomatism by Na–Si-rich fluids (Pohlner *et al.*, 2025). Although we did not attempt to characterize each composition in detail, our STEM–EDS measurements, which should have captured such a micron-scale area without mixed analysis, revealed two distinct groups with different Na content (Na-rich cluster: CLR01 and CLR02; Na-poor cluster: CLR03 and CLRTS_04; Fig. 2b). Since the three separated grains (CLR01, CLR02, CLR03) are characterized by similar compositions with our EPMA analysis (Fig. 2a), these clusters may represent the submicron-scale compositional heterogeneity rather than grain-to-grain variation. This compositional difference is thus likely to reflect the metasomatic Na enrichment. A detailed discussion on the metasomatism is out of the scope of this manuscript, but at least we could argue that our xenolith sample experienced a similar metamorphic–metasomatic history to other Navajo eclogite samples.

Record of heating

Disordered omphacite

The omphacite specimens are almost disordered, even though the critical temperature of the order–disorder transition in omphacite is ~865 °C, which is far higher than the previously estimated peak metamorphic *T*: ~620 °C (Hernández-Uribe & Palin, 2019). The critical

Downloaded from academic.oup.com/petrology/article/67/10/egag092/8913147 by guest on 30 October 2026

Table 1 Crystallographic data from single crystal structure refinements of omphacite.

	CLR01	CLR02	CLR03
Structural formula[1]	$(Ca_{0.39}Na_{0.61})^{M2}(Mg_{0.35}Fe_{0.23}Al_{0.42})^{M1}Si_2O_6$		
Space group	*C*2/*c*	*C*2/*c*	*C*2/*c*
a, Å	9.5742(3)	9.5798 (4)	9.5807 (4)
b, Å	8.7456 (3)	8.7528 (3)	8.7550 (3)
c, Å	5.25600 (17)	5.2569 (2)	5.2577 (2)
β, °	106.972 (3)	106.940 (4)	106.937 (4)
V, Å^3	420.93 (2)	421.67 (3)	421.88 (3)
R_{int}	0.0395	0.0402	0.0335
R_1 ($I > 2\sigma(I)$)	0.0429	0.0356	0.0322
wR_2 ($I > 2\sigma(I)$)	0.1023	0.0931	0.0850
R_1 (all data)	0.0518	0.0388	0.0350
wR_2 (all data)	0.1089	0.0958	0.0882
goodness of fit	1.188	1.149	1.157
Mean bond length, Å^3			
<M1–O>	2.0017 (4)	2.0038 (4)	2.0048 (4)
<M2–O>	2.4899 (3)	2.4917 (4)	2.4903 (3)

[1]The average composition of EPMA data (in Table S2) was used for all crystals.

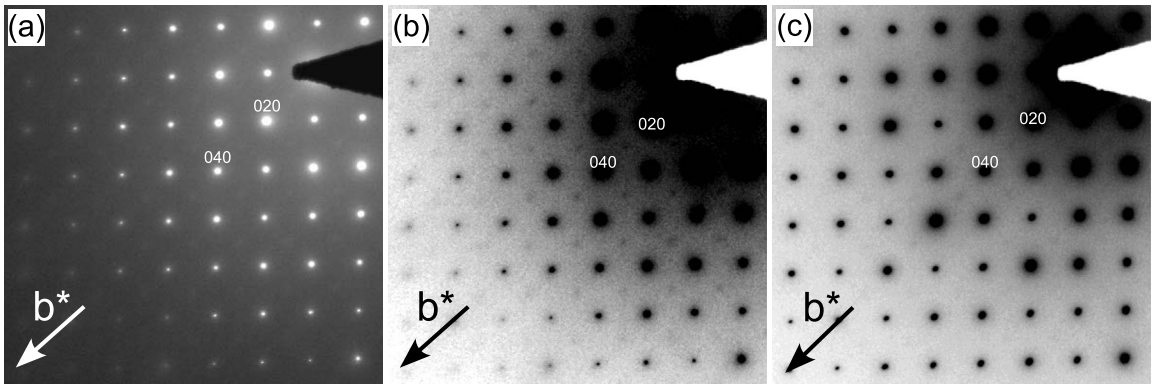


Figure 6 SAED patterns of the omphacite (Z = [001], sample CLR03). (a) Representative SAED pattern. (b) Same image but lightness inversion and brightness-contrast adjustment were applied for emphasizing weak reflections. Diffuse scattering of 0k0 (k = odd) is observed. (c) SAED pattern with 3° beam precession for the same area. The diffuse scattering almost disappears.

temperature generally decreases in Fe-rich omphacite, but omphacite with a similar aegirine component as our samples ($X_{aeg} \sim 0.15$) from the Nevado-Filábride Complex (Spain; peak metamorphic *T*: ~630 °C) was still characterized by long-range order (Cámara *et al.*, 1998). Thus, the xenolith-forming omphacite should have retained long-range order at the end of the subduction.

Previous experimental studies show that cation disordering in omphacite is completed within a few weeks at >900 °C (Fleet *et al.*, 1978; Carpenter, 1982*a*). As this timescale is far shorter than the timescales of relevant geological processes, omphacite can be disordered if the rock was rapidly heated up, even when the mineral assemblage infers equilibrium at low-*T* conditions. Thus, the absence of long-range order in our samples is best explained by a later-stage thermal pulse. Although the critical temperature of Fe-rich omphacite should be somewhat lower than that of Fe-free omphacite, the disordering experiments by Cámara *et al.* (1998) reported the persistence of some ordering at 800 °C in the Nevado-Filábride omphacite, suggesting that the critical temperature is not much affected by the Fe content. Therefore, we infer that omphacite in our xenolith sample experienced rapid heating to >800 °C.

Amorphous phase in omphacite

The amorphous phase found in omphacite (Fig. 7a) is explained by quenched silicate melt with a felsic composition, as the spacing in the SAED pattern (3–4 Å; Fig. 7c) is consistent with that observed in felsic silicate glass interpreted as quenched melt (3.8 Å; Masch *et al.*, 1985). Another piece of evidence is the abundant dislocations in the accompanying Ca-rich omphacite (Fig. 7c); because dislocation-rich omphacite is known to grow from melt probably under thermal stress (Pollok *et al.*, 2014), this Ca-rich omphacite would have grown from the coexisting melt.

The submicron-scale morphology of the array might be comparable to string-of-beads microstructure indicating the former presence of melt (e.g. Holness & Sawyer, 2008). However, such melt-film pseudomorphs in previous literature are tens of micrometers wide, and they mostly occur in the rock matrix rather than within single crystals (Cesare *et al.*, 2015), which does not agree with our observation (Fig. 7). Although submicron-scale silicate-melt pockets have recently been reported in a TEM-based study of peridotite xenoliths from Romania (Lange *et al.*, 2023), they are even located along grain boundaries between different mineral phases without forming arrays. By

Downloaded from academic.oup.com/petrology/article/67/10/egag092/8913147 by guest on 30 October 2026

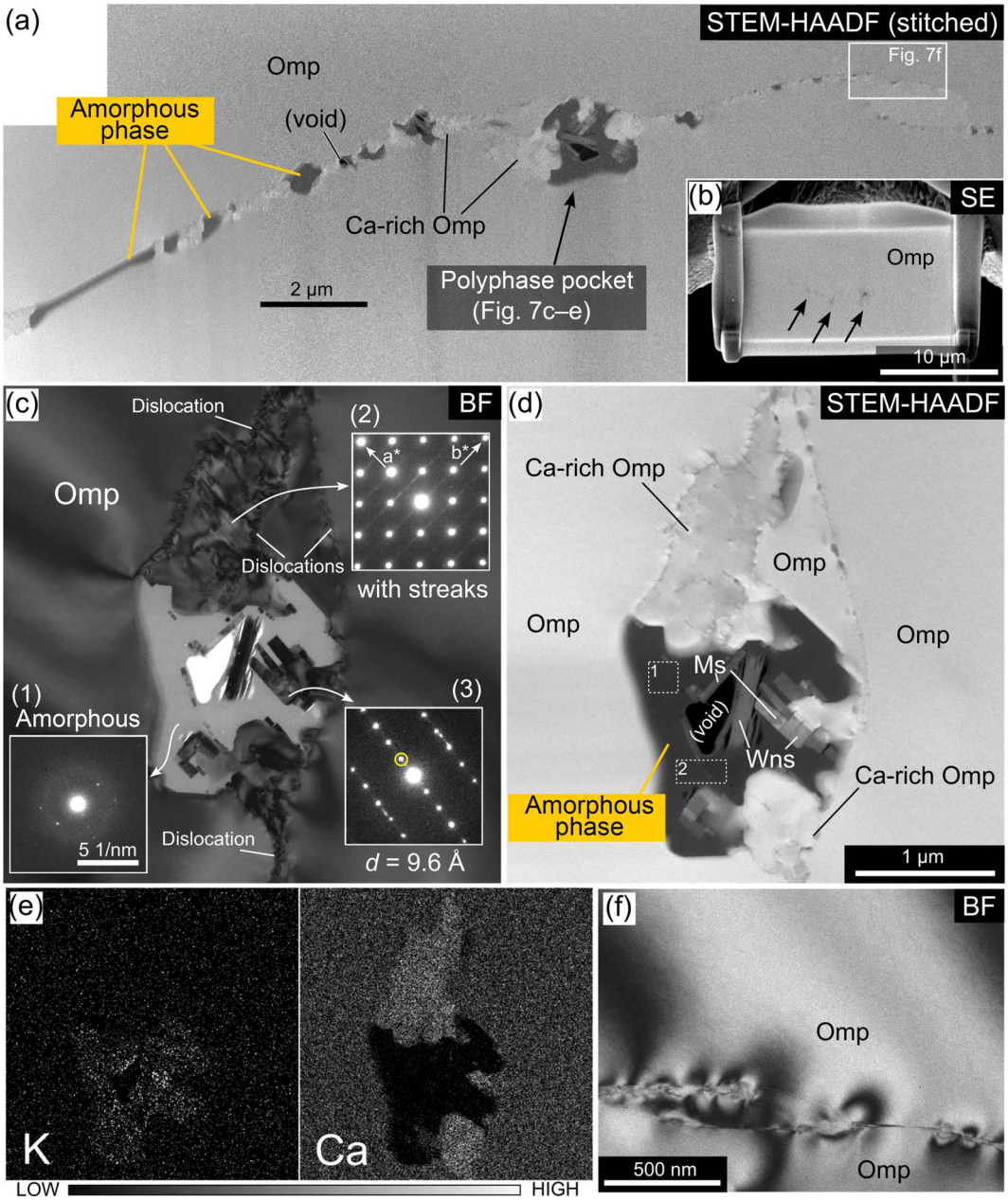


Figure 7 Amorphous phase preserved in one of the separated omphacite grains (CLR03). (a) Stitched STEM-HAADF image of the array of the amorphous phase, Ca-rich omphacite, and void. (b) Secondary electron image of the foil specimen (microphotograph taken in the FIB apparatus). The arrows indicate the amorphous phase. (c) BF-TEM image of the polyphase pocket presented in (a). As insets, representative SAED patterns are also presented: (1) diffuse ring (~3–4 Å) demonstrated that the phase is amorphous; (2) SAED pattern of coexisting Ca-rich omphacite (Z = [001]) shows streaks parallel to the b* direction, reflecting the presence of stacking defects on the (010) plane; (3) spacing of d = 9.6 Å revealed the presence of wonesite (Wns). (d) STEM-HAADF image of the same area. The dashed squares indicate the areas for the compositional analysis with STEM–EDS. (e) X-ray intensity maps of the same area (K, Ca). (f) BF-TEM image of the dislocation presented in (a).

contrast, arrays of micron- to submicron-scale aqueous fluid inclusions commonly occur within single crystals along their growth planes (as a primary type) or along healed cracks (as a secondary type) (e.g. Van den Kerkhof & Hein, 2001; Lange *et al.*, 2023). If a given single crystal encompassing such an array of aqueous fluid pockets is heated up, flux melting may locally occur around the fluid pockets, possibly forming a string of 'melt beads' as in our observation.

Although it remains possible that the observed glass-bearing microstructure was formed by external melt infiltration, we here favor the interpretation that localized flux melting of the host omphacite occurred where the array of aqueous fluid inclusions or films was already present. Indeed, Ca-rich omphacite in the array can be readily interpreted as a peritectic phase of flux melting of omphacite-dominated assemblages (Laurie & Stevens, 2012; Liu *et al.*, 2023), which preferentially nucleated at the omphacite–omphacite–melt junctions. Based on the observed texture, the melting reaction could be expressed as omphacite + solute-bearing aqueous fluid = felsic melt + Ca-rich omphacite ± phyllosilicates, although one cannot rule out that

Downloaded from academic.oup.com/petrology/article/67/10/egag092/8913147 by guest on 30 October 2026

Table 2 Chemical compositions of amorphous materials/phases measured with STEM-EDS.

	IAM in a Lws pseudomorph (Fig. 4f)[2]		Amorphous phase in Omp (Fig. 7d)[3]	
Area no.	**1**	**2**	**1**	**2**
Normalized weight percent (without H_2O)				
SiO_2	59.68	57.26	72.85	75.39
TiO_2	1.21	1.83		
Al_2O_3	16.09	14.11	18.61	17.89
FeO[1]	8.44	8.33		
MnO	0.33	0.35		
MgO	1.92	n.d.		
CaO	7.99	7.36	0.65	0.63
Na_2O	0.92	n.d.	4.86	3.25
K_2O	n.d.	n.d.	3.03	2.84
ZnO	1.48	3.50		
SO_3[1]	1.93	7.25		
Total	99.99	99.99	100.00	100.00

n.d., not determined.
[1]Total Fe as Fe^{2+}, and total S as S^{6+}.
[2]Measured at GRC.
[3]Measured at BGI.

other eclogite-forming phases (e.g. garnet, lawsonite) were involved in the reaction. Since the host omphacite is a separated grain, it is unclear whether these additional possible reactants were located sufficiently close to the omphacite grain. At least, the occurrence of K-bearing phyllosilicates and the selective K uptake into the amorphous phase imply the involvement of some K source, but the most promising candidate for the source is the aqueous fluid inclusions in any case, because phengite is not found in our xenolith sample. The K-bearing aqueous fluid might have derived from eclogite-facies metasomatism before the heating event.

The *P*–*T* conditions for melting are a matter of interest, but it is not straightforward to obtain the actual melt composition——the essential information for further thermodynamic analysis. The void and daughter minerals in the amorphous phase suggest fluid exsolution and crystallization from/of the melt, which may have modified its original composition. In addition, potential Na loss during STEM–EDS measurements of hydrous silicate glass might also hamper the accurate compositional analysis (e.g. Morgan & London, 2005). It would be also difficult to determine the *P*–*T* conditions based on phyllosilicates in the amorphous phase. For example, wonesite was originally reported from an amphibolite-facies metamorphic rock (Spear *et al.*, 1981; Spear, 1982), but a recent experimental study shows that wonesite can be stable also with eclogite-facies mineral assemblages at $T > 600$ °C and $P = 3$ GPa (Lakey & Hermann, 2022). One also cannot completely rule out that their crystallization occurred in a metastable manner in such a small space (Ferrero & Angel, 2018; Ferrero *et al.*, 2026). Consequently, we are compelled to assume that the maximum temperature for this xenolith would have exceeded the wet solidus of eclogite, or 700–800 °C depending on the pressure lower than 3.7 GPa (Schmidt & Poli, 1998; Kessel *et al.*, 2005,), or the estimated peak metamorphic pressure (Hernández-Uribe & Palin, 2019).

Decomposed lawsonite with IAM

The IAM in the lawsonite pseudomorph (Fig. 4f) has distinctive features that are unlikely to represent pristine quenched melt. Although having similar spacing in the SAED pattern (3–4 Å), the appearance and chemical composition are different between the IAM (uneven surface, incomparable composition to known phases) and the amorphous phase preserved along dislocations in omphacite (smooth surface, felsic-melt-like composition). Notably, the banding texture consisting of nanoparticle aggregates in the IAM resembles microscopic features of corroded glass (Bunker, 1994; Salviulo *et al.*, 2004; Schalm & Anaf, 2016). We thus regard the IAM found in the lawsonite pseudomorph as corroded silicate glass.

Considering the confirmed series of rapid heating and quenching, the silicate glass before corrosion is also naturally interpreted as a quenched silicate melt. The presence of former silicate melt in the lawsonite pseudomorph suggests that lawsonite breakdown was accompanied by partial melting, rather than proceeding entirely through subsolidus replacement. Since lawsonite hosts large amount of H_2O (~11.5 wt %), the xenolith would have experienced dehydration melting of lawsonite. As lawsonite itself contains only trace amounts of alkalis, a substantial amount of Na must have been added externally. Such a gain of alkalis from surrounding minerals is common in lawsonite pseudomorphism (e.g. Hamelin *et al.*, 2018).

The morphology of the micron-scale crystals found in the pseudomorph constrains the crystallization sequence. Plagioclase is subhedral to anhedral, whereas zoisite and mica are euhedral, suggesting that plagioclase crystallized from the residual melt after most of the zoisite and mica already crystallized. Plagioclase is able to grow in melt with temperature increase if consuming zoisite (e.g. Schmidt & Poli, 2004), but this reaction is not applicable because there is no textural evidence confirming zoisite dissolution. The plagioclase crystallization was thus driven by cooling in the zoisite stability field. Since plagioclase is unlikely to grow stably at eclogite-facies conditions, its crystallization must have occurred at significantly lower pressures. The upper pressure limit of the plagioclase stability field could be estimated by the following univariant reaction in the Na_2O–CaO–Al_2O_3–SiO_2–H_2O system (Wayte *et al.*, 1989):

$$\mathrm{Pl} + \mathrm{H_2O} = \mathrm{Zo} + \mathrm{Jd} + \mathrm{Ky} + \mathrm{Qz}.$$

We calculated this reaction by using THERMOCALC (with a solution model for plagioclase in the igneous set: Holland *et al.*, 2022).

Downloaded from academic.oup.com/petrology/article/67/10/egag092/8913147 by guest on 30 October 2026

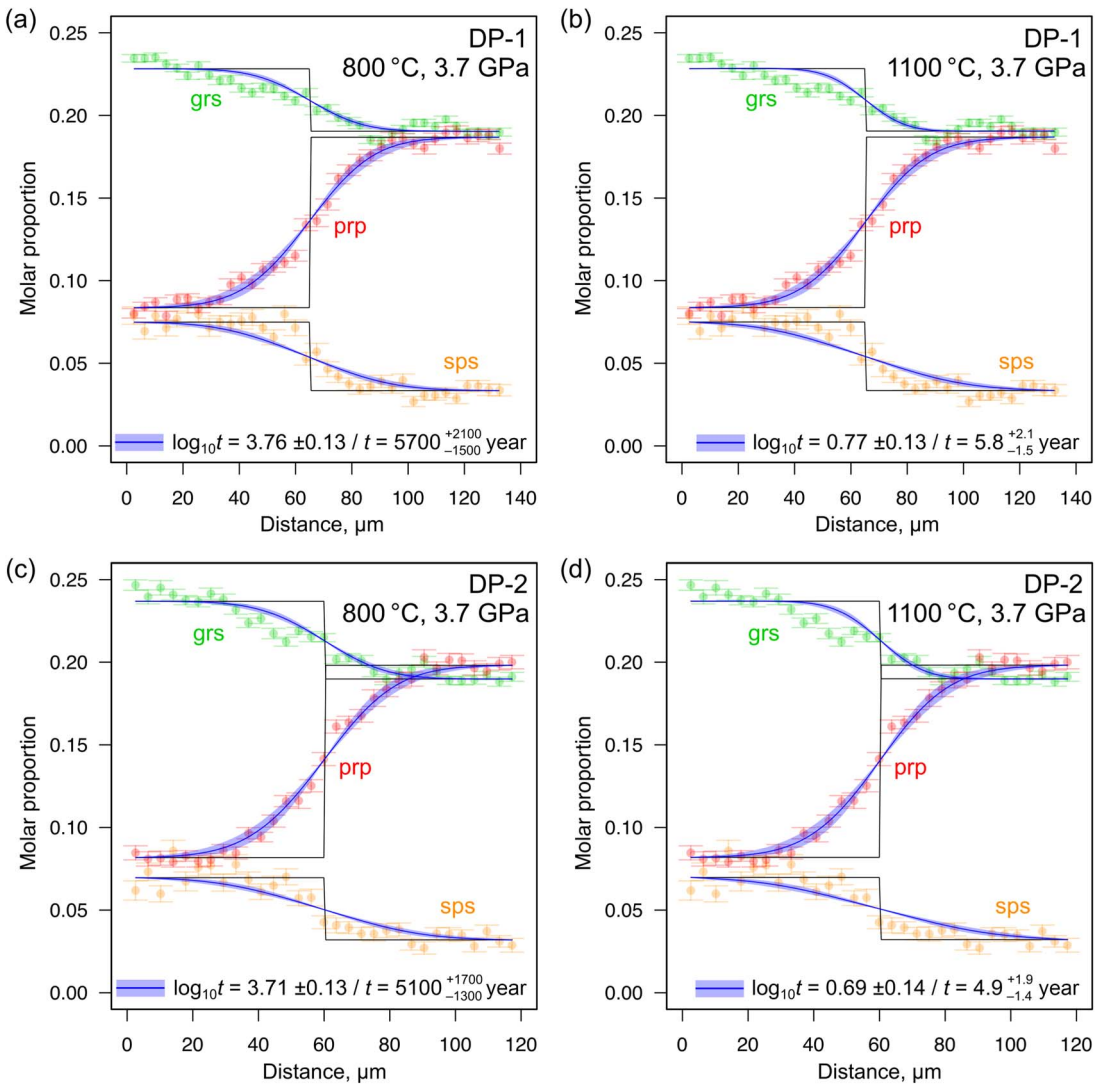


Figure 8 Results of multicomponent diffusion modeling in garnet. (a, b) Results for DP-1 at $T = 800$ °C and 1100 °C, respectively. (c, d) Results for DP-2 at $T = 800$ °C and 1100 °C, respectively. The pressure condition is fixed to $P = 3.7$ GPa in all cases. Uncertainty of time ($\pm 1\sigma$) is derived from curve fitting.

Speculating that the solidus temperature is around 600–800 °C, we obtained the maximum possible pressure of 1.7–2.2 GPa when the partially molten xenolith was cooled down.

The maximum heating temperature may be constrained from the upper temperature limit of the zoisite stability field, but the estimation is not straightforward. Even though zoisite lacks any obvious dissolution texture, it might have been possible that the temperature was transiently above the zoisite stability field, if heating was sufficiently rapid or zoisite dissolution rate was slow enough. If forced to say, however, the maximum possible temperature would have been roughly 1050–1200 °C at >2 GPa in the $CaO–Al_2O_3–SiO_2–H_2O$ system (Schmidt & Poli, 2004), assuming that it did not far exceed the zoisite stability field under wet or dry conditions.

Timescale and mechanism of heating

Based on the discussion above, it is evident that our xenolith sample experienced rapid heating to >800 °C. Here, we constrain the heating timescale from diffusion modeling of garnet. Assuming that Grt-2 was formed by metasomatic replacement of Grt-1 just before the heating event, two diffusion profiles from Grt-1 to Grt-2 (Table S12) were modeled with constant *P*–*T* conditions. The pressure was always fixed to that of the peak metamorphic condition (3.7 GPa). Note, that the obtained diffusion timescale in our modeling is a maximum possible estimate because there may have been a significant temporal gap between the timings of Grt-2 formation and subsequent heating. In addition, a potential decompression from 3.7 GPa during heating is not considered in our modeling, which leads to an underestimation of cation diffusivity due to the positive activation volume.

First, we set the heating (annealing) temperature at 800 °C. As a result, we obtained the best-fit timescales of $5700 + 2100/-1500$ years (DP-1; Fig. 8a) and $5100 + 1700/-1300$ years (DP-2; Fig. 8c). We can safely argue that heating must have been $<10^4$ years regardless of the heating temperature, since the modeled temperature of 800 °C is the minimum estimate.

Such rapid heating is only possible if magma is involved, probably beneath the subcontinental lithospheric mantle. However, if the agent was a deep-sourced magma (i.e. those originated from

Downloaded from academic.oup.com/petrology/article/67/10/egag092/8913147 by guest on 30 October 2026

asthenosphere), the magma temperature could have been far higher than 800 °C. For example, the source of minette magmatism in the Navajo Volcanic Field is thought to have formed by melting of metasomatized lithospheric mantle beneath the plateau (Carlson & Nowell, 2001), whose temperature must have exceeded 1100 °C based on phase equilibria (Esperança & Holloway, 1987; Smith *et al.*, 2004). If we set the modeled temperature at 1100 °C instead of 800 °C, we obtained the best-fit timescales of $5.8+2.1/-1.5$ years (DP-1; Fig. 8b) and $4.9+1.9/-1.4$ years (DP-2; Fig. 8d). These results suggest that the heating timescale was far shorter than 10^4 years, probably <10 years, if a deep-sourced magma directly interacted with the xenolith.

Considering all the observations, we conclude that our xenolith sample was rapidly brought up by a deep-sourced magma to a shallow level at least less than ∼60 km (equivalent to ∼2 GPa). This process caused rapid heating, local flux melting of the xenolith, and dehydration melting of lawsonite. Quenching to subsolidus temperatures would have occurred after this magmatic transportation. The estimated heating timescale (<10 years) is consistent with a physical requirement of magma ascent rate for bringing up the ∼20 cm-sized xenolith; previous studies estimated the minimum ascent rate required for transporting such xenoliths at $\sim10^{-1}$ m/s (Spera, 1980; O'Reilly & Griffin, 2010), corresponding to ∼60 km/week.

Interpretation of selected localized reactions

We observed several microstructures whose formation mechanisms cannot be explained only by rapid heating. By focusing on several records of localized reactions, we here elaborate on the comprehensive history of the xenolith exhumation.

Occurrence of Mg-rich phyllosilicate

Although the Mg-rich phyllosilicate, found in lawsonite pseudomorphs (Figs 4b, d and 5d–h), may be labeled as aluminous serpentine by considering its structure, we call the phase '7 Å-chlorite' in accordance with convention. The stability of such phyllosilicate with chlorite-like compositions (see the compositional range shown in Fig. S6; Velde, 1973) but with 7 Å basal spacing (traditionally called either 7 Å-chlorite or 'septechlorite') has been investigated experimentally. Notably, 7 Å-chlorite has been reported only as a hydrothermal reaction product below ∼500 °C (Yoder, 1952; Nelson & Roy, 1958; Yamanaka & Bodine, 1971; Velde, 1973; Tamura, 1982), which is below wet solidus of any rock type (unless abundant flux elements are present as in pegmatite). A 7 Å-chlorite is also known to occur as a precursor phase of normal (or 14 Å) chlorite (e.g. Cho & Fawcett, 1986), but it is unclear whether a complete reversal from 14 Å- to 7 Å-chlorite is possible. Hence, it is highly questionable whether the phase was directly crystallized from melt.

Constraints from an aspidolite-forming reaction

Another notable feature of the lawsonite pseudomorph is the occurrence of aspidolite. It forms zoisite-free halo together with 7 Å-chlorite and plagioclase (Fig. 5a–f). One straightforward interpretation of the halo formation is as follows: lawsonite + omphacite were reacted to produce zoisite + aspidolite +7 Å-chlorite + albite. To confirm if this reaction is possible to occur, we first explored algebraically allowed reactions in the relevant compositional space. We considered the following phases in the Na_2O–CaO–MgO–Al_2O_3–SiO_2–H_2O (NCMASH) system: lawsonite, zoisite, aspidolite, albite, H_2O (as end-member compositions), chlorite (assumed by $\sim clc_{60}\ sud_{40}$), and omphacite (assumed by $\sim di_{40}\ jd_{60}$). As a result, we found only one possible reaction under which lawsonite + omphacite are reactants and all the other phases are involved:

$$\mathrm{Lws + Omp + Asp = Zo + Chl + Ab + H_2O.}$$

However, this reaction must consume aspidolite, which contradicts our premise that aspidolite was a reaction product. It seems impossible to balance MgO if both aspidolite and 7 Å-chlorite were to form simultaneously.

Instead, one may interpret that 7 Å-chlorite is a secondary mineral that replaced preexisting melt-derived silicate glass, which is generally vulnerable to hydrothermal alteration. This idea, although somewhat speculative, is invoked by its small grain size (≪1 μm) and unique fibrous morphology with abundant porosity and random orientation—the common features of low-*T* altered silicate glass (e.g. Ralston *et al.*, 2023; Leroux *et al.*, 2024). If the area filled by 7 Å-chlorite aggregates originally consisted of silicate melt, a reaction producing aspidolite + zoisite + melt + albite from lawsonite + omphacite is expected. Alternatively, if plagioclase was a peritectic phase of a later reaction of omphacite + melt (as suggested by the proximity of 7 Å-chlorite to omphacite; Fig. 5d), the aspidolite-forming reaction may have produced only aspidolite + zoisite + melt. In any case, however, scarce information on the original melt composition hampers a simple algebraic test.

To verify if these aspidolite- and melt-forming reactions can occur, we performed thermodynamic modeling with THERMOCALC. Because of the lack of the mixing model for Mg–Fe-aspidolite, we must have ignored FeO from the system. We adopted the NCMASH system with solution models for omphacite (metabasite set: Green *et al.*, 2016), plagioclase (igneous set: Holland *et al.*, 2022), melt and aqueous fluid (igneous set: Holland *et al.*, 2018; Green *et al.*, 2025). Since this aqueous fluid model considers silicate material dissolution at high-pressure conditions, this model is the best choice to describe wet melting of high-pressure metamorphic rks. Lawsonite, zoisite and aspidolite ('naph' in THERMOCALC) were considered as end-member phases. As a result, we found the following univariant and divariant reactions:

$$\mathrm{Lws + Omp = Zo + Asp + Pl + H_2O\text{-saturated melt + solute-bearing\ aqueous\ fluid,\ or}}$$

$$\mathrm{Lws + Omp = Zo + Asp + H_2O\text{-saturated melt + solute-bearing\ aqueous\ fluid.}}$$

These reactions are visualized in the *P*–*T* space (Fig. S8). Our calculation shows that these reactions were able to occur when the xenolith was transported to a shallower level after the eclogite-facies metamorphism.

Previous studies suggest that the occurrence of Na-rich magmatic aspidolite (with ∼6 wt % Na_2O) is limited as mono- or polymineralic inclusions in chromite (see compilation by Costa *et al.*, 2001). Although thermodynamic requirements for the aspidolite stability remains unclear, such a specific mineral-enclosed system may stabilize an H_2O-rich environment, thereby leading to the aspidolite formation (Schiano *et al.*, 1997). In the case of our sample, aspidolite is accompanied by omphacite grains enclosed in lawsonite pseudomorphs, and the promising reactions suggested above are

Downloaded from academic.oup.com/petrology/article/67/10/egag092/8913147 by guest on 30 October 2026

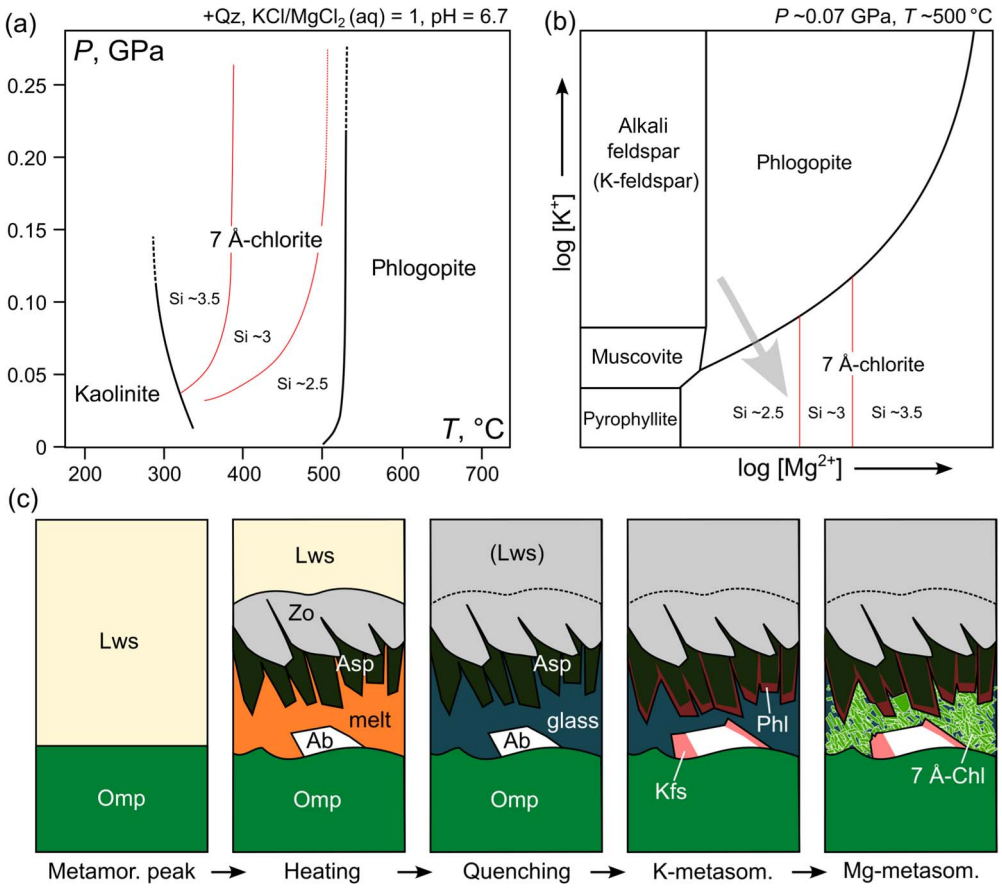


Figure 9 Stability and genesis of 7 Å-chlorite, phlogopite, and alkali feldspar in the zoisite-free halo (Fig. 5). (a, b) Stability field of the relevant phases in the KMASH system constrained by experiments (modified after Yamanaka & Bodine, 1971). The red lines indicate formal thresholds among penninite (Si = 3.5 a.p.f.u.), clinochlore (Si = 3.0 a.p.f.u.), and sheridanite (Si = 2.5 a.p.f.u.). the thick gray arrow illustrates the shift in fluid composition that explains our observation. (c) Schematic figure depicting the proposed formation process of the zoisite-free halo.

involved by aqueous fluid and H_2O-saturated melt. This consistency validates our interpretation of the textural formation history.

Our discussion so far corroborates that 7 Å-chlorite is a secondary mineral, which could have replaced melt-derived silicate glass. The expected melt compositions are basically felsic, only with <10 wt % MgO (Fig. S8), suggesting Mg gain for the replacement by 7 Å-chlorite (>25 wt % MgO; Table S11). Considering that Mg-rich phyllosilicate laths are evenly distributed in lawsonite pseudomorphs, not only in the zoisite-free halo (Fig. 4a, b, d), it is natural to infer that they are also originally melt-derived glass suffering from a similar alteration process. In our view, so far, two different processes operated for the 'lawsonite pseudomorphism': lawsonite breakdown with partial melting–quenching, and low-temperature alteration by Mg-rich fluid.

Minor K-metasomatism

Here, we further discuss the origin of K-rich phases in the zoisite-free halo: phlogopite and alkali feldspar (K-feldspar). The formation of phlogopite rims around aspidolite and alkali-feldspar attachment to albite imply a metasomatic K enrichment (e.g. Banno *et al.*, 2005), but our xenolith sample does not have any other mineralogical evidence of K-rich fluid infiltration such as secondary phengite formation. One may envisage that if K-rich fluid infiltrated into partially molten rock, the incompatible K component will be partitioned into the melt to suppress K-rich phase nucleation where partial melt is absent. However, this idea contradicts to our observation that mica and plagioclase found in lawsonite pseudomorphs have almost K-free compositions. If these phases coexisted with melt and were to have suffered from significant K-metasomatism, their compositions would also have shifted. Alternatively, K-rich phases in the zoisite-free halo may have crystallized after the glass formation as devitrified crystals, but it remains uncertain whether this scenario explains such a selective occurrence of K-rich phases.

A previous experimental study on the stability of 7 Å-chlorite and phlogopite provides a key to understanding this phenomenon. Yamanaka & Bodine (1971) investigated their equilibrium relation in the K_2O–MgO–Al_2O_3–SiO_2–H_2O (KMASH) system with quartz saturation by changing P–T conditions ($P < 0.25$ GPa and $T = 300$–700 °C) and chemical compositions of the starting solid materials and solutions (the ratio of KCl to $MgCl_2$). They confirmed that the transition from 7 Å-chlorite (stable at lower T) to phlogopite (stable at higher T) occurs at $T = 450$–550 °C with a wide range of fluid compositions at ~0.07 GPa. In addition, Si-poor 7 Å-chlorite (e.g. Si <3 a.p.f.u. as in the majority of our samples) is found to be stable with relatively Mg-rich fluids, only at near the phlogopite stability field ($T = 450$–550 °C), whereas those enriched in Si are stable at lower temperature (Fig. 9a). They also showed that 7 Å-chlorite of variable compositions, phlogopite, and alkali feldspar are transformable to each other by changing fluid compositions at constant P–T conditions (Fig. 9b).

Downloaded from academic.oup.com/petrology/article/67/10/egag092/8913147 by guest on 30 October 2026

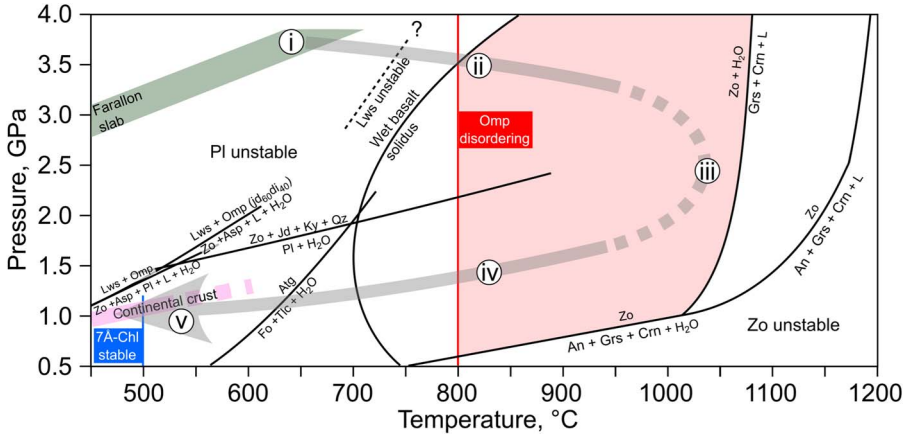


Figure 10 Integrated *P–T* scenario of the thermal pulse (gray thick arrow). The green shaded band indicates the probable *P–T* conditions along the Farallon slab surface (Hernández-Uribe & Palin, 2019; Pohlner *et al.*, 2025). The red shaded area represents possible *P–T* conditions during the thermal pulse (wet zoisite melting is tentatively assumed to limit the upper temperature). The red and blue lines indicate the estimated temperature for omphacite disordering (>800 °C; see the subsection 'Record of heating') and stability limit of 7 Å-chlorite formation (<500 °C; see the subsection 'Interpretation of selected localized reactions'), respectively. The pink shaded band indicates a modeled geotherm of the continental crust beneath the Colorado Plateau (13 °C/km; Worthington *et al.*, 2024). The wet basalt solidus, zoisite breakdown reactions, and antigorite breakdown reactions are also presented (Ulmer & Trommsdorff, 1995; Schmidt & Poli, 2004; Kessel *et al.*, 2005). Other solid black lines are those calculated in this study. Note, that the actual breakdown conditions of lawsonite (dotted black line) are not strictly determined but could be at slightly lower temperature than wet basalt solidus (e.g. Schmidt & Poli, 1998).

These experimental results might not be directly applicable to our case because of the less constrained reaction pressure. Nevertheless, if the effect of pressure variation is not significant (as suggested in Fig. 9a), such a reaction relationship between 7 Å-chlorite and phlogopite will explain the morphological variation of 7 Å-chlorite found in the zoisite-free rim, or the reason why some grains adjacent to phlogopite are thick tabular in shape (Fig. 5e, f). Since phlogopite can readily transform into 7 Å-chlorite with Mg metasomatism and/or cooling, the precursor of the 7 Å-chlorite in the zoisite-free rim was not necessarily restricted to the melt-derived glass; rather, some of the preexisting phlogopite grains may have been also replaced by 7 Å-chlorite, which succeeded their original crystal shapes. At the same time, tiny 7 Å-chlorite laths would have formed by replacing the remaining glass, thereby forming the morphological contrast. If this interpretation is correct, the overgrowth of phlogopite rim must have preceded the 7 Å-chlorite formation.

Taken together, we propose that two successive alteration events by K- and Mg-rich fluids occurred after the glass formation (Fig. 9c). The preceding K-metasomatism was not very significant as replacing all parts of the glass, and subsequent Mg-metasomatism (and perhaps cooling) obliterated some minor records of K-metasomatism. Furthermore, there was likely spatial variation in the probability of K-rich phase formation with such minor K-metasomatism, depending on the local fluid composition, the resistance to alteration, and the presence/absence of the potential nuclei such as magmatic aspidolite.

Unresolved localized reactions

One undiscussed feature is how Na and other components were conveyed into decomposing lawsonite. The likely source of Na is the matrix-forming omphacite, but there is no evidence of re-equilibration of omphacite walls of polyhedral lawsonite pseudomorphs (Fig. 1f). The Na input might be balanced by a reaction forming the veinlets (amphibole + plagioclase + Ca-rich omphacite) that crosscut the matrix-forming omphacite (Fig. 1g, h). The mineral assemblage and compositions of the veinlets resemble those of retrograded eclogite that experienced fluid-assisted, open-system breakdown of omphacite at relatively high-*T* conditions (O'Brien, 1993; Martin & Duchêne, 2015; Feng *et al.*, 2021; Zertani *et al.*, 2024). We thus envisage that the veinlets were synchronously formed when lawsonite was partially molten, by replacing part of matrix-forming omphacite along microcracks, thereby providing/extracting some elements into/from the adjacent lawsonite pseudomorph. Nonetheless, scarce information on the original melt composition in lawsonite pseudomorphs and the unquantified reacting volume of the matrix-forming omphacite hamper discussion of the detailed mass transfer during lawsonite melting.

Another unresolved feature is the occurrence of dissolved pores and amphibole (other than those in the veinlets) in matrix-forming omphacite (Fig. 1c–e). The absence of dissolved pores in some omphacite grains enclosed in garnet may suggest dissolution of omphacite after some extent of garnet formation. Considering that the pore formation has not necessarily been accompanied by radial cracks from lawsonite pseudomorphs (Fig. S3), the dissolution was likely not coeval with lawsonite breakdown; their formation was perhaps linked to eclogite-facies metasomatism or later alteration processes. Additional petrological investigation will be required to understand the dissolution mechanism as well as amphibole precipitation processes.

Integrated scenario of the xenolith exhumation

Combining our discussions of heating-to-quenching records and subsequent metasomatic fingerprints, we here suggest the whole picture of the xenolith exhumation history. Along the integrated *P–T* path summarized in Fig. 10, a series of key events can be described as follows.

i) Farallon slab was subducted to eclogite-facies conditions, accompanied by multiple metasomatic events. The Mg-rich garnet (Grt-2) was formed at a certain stage during

Downloaded from academic.oup.com/petrology/article/67/10/egag092/8913147 by guest on 30 October 2026

the metasomatism. The metamorphic peak conditions were estimated at ∼620 °C, 3.7 GPa.

ii) Part of eclogitized Farallon slab was entrained by a deep-sourced magma, broken into small pieces, and rapidly heated to >800 °C. Lawsonite was decomposed with dehydration melting, whereas omphacite suffered from cation disordering. The eclogitized slab fragments also locally experienced flux melting where free aqueous fluid was available. At some point, aspidolite was locally formed as a peritectic phase of the melt-forming reaction of omphacite + lawsonite.

iii) The eclogite fragment was transported to a shallower depth as a xenolith by the deep-sourced magma. The maximum temperature is not firmly constrained, but probably significantly higher than 800 °C.

iv) The eclogite xenolith started to cool down due to a diminishing magma supply. This should have occurred at subsurface conditions to explain the field observation (i.e. no magmatic evidence on surface) and the sufficiently high-T condition for the upcoming metasomatism forming Si-poor 7 Å-chlorite (∼500 °C) consistently, but the depth must have been at least shallower than ∼60 km to ensure plagioclase stability. Note, that this condition can be achievable at lower crust or near the Moho, assuming a reasonable geotherm of ∼13 °C/km (Worthington *et al.*, 2024). The cooling rate was sufficiently fast that some part of silicate melt was preserved as glass.

v) Hydrothermal alteration of hydrous silicate glass. The formation of 7 Å-chlorite should have occurred at ∼500 °C or marginally lower temperatures. This stage would have been followed by, or proceeded synchronously with, the final explosive exhumation to the surface.

As for the final explosion, our observations do not provide any novel constraint. Nonetheless, our proposed scenario is consistent with the final explosion of antigorite serpentinite matrix in terms of the physical requirement of hydrofracturing ($P < 2$ GPa).

It should be noted that we cannot obtain the total lifespan of the subsurface alteration stage; this information would be necessary to know the heat source of the final explosion. It remains unclear whether there was a seamless transition from magmatic to non-magmatic exhumation, which may have been possible if the heat source is identical to the xenolith-transporting magma itself. By contrast, if there was a significant time lag between the subsurface xenolith quenching and final explosion, the heat source was perhaps different magma from the xenolith-transporting one.

Implication

Based on crystallographic and micropetrological evidence, we have shown that Navajo eclogite xenoliths were transported from the bottom of the subcontinental lithospheric mantle by a deep-sourced magma. Since many of the earlier studies did not explicitly consider this process, the previously reported petrological, geochemical, and geochronological data may need to be re-evaluated.

Our finding contributes to a more complete picture of the terminal stage of Farallon slab subduction by providing a fundamental T–t constraint on the eruption dynamics related to the flat slab collapse. Nonetheless, the origin of the magma that transported slab fragments has not been resolved yet. The magma may have either been generated by asthenosphere invasion between the sinking slab and subcontinental lithospheric mantle (on the analogy of the proposed formation mechanism of minette magma), or originated from deeper asthenosphere beneath the slab (like kimberlite magmatism). It would be difficult to solve this problem based only on a thermal history recovered from the single eclogite xenolith. The key to understanding this transient magmatic process will lie on the spatiotemporal relationship among serpentinite dehydration in the Farallon slab, intraslab fluid flow, thermal field changes due to slab foundering or potential asthenospheric upwelling, and metasomatic agent at the subsurface alteration stage.

Another open question is why slab fragments were not exhumed to the surface with a single magmatic eruption. One simple interpretation is that the magma supply rate was not sufficient for the sampling magma to reach the surface (possibly sort of a 'failed' eruption; Giuliani *et al.*, 2016). Alternatively, a small amount of magma could have reached the surface, but lagging of the xenolith arrival potentially allowed its subsurface settlement (Russell & Jones, 2023). The prevalence of this sort of incomplete eruption must be assessed in future studies to understand the nature of magma–rock interaction at mantle depths.

Furthermore, this study has the potential to enhance our knowledge of microstructural formation in rapidly heated slab material. As far as we know, this is the first-ever report of dehydration melting of lawsonite; our petrological and crystallographic description is invaluable as an extreme example of hydrous phase breakdown and pseudomorphism. More detailed investigation of the intra-xenolith mass transfer during lawsonite pseudomorphism will facilitate discussion about fluid-involved disequilibrium reaction processes in high-P metamorphic rocks.

Supplementary data

Supplementary data are available at *Journal of Petrology* online.

Acknowledgements

The authors express their deep appreciation to Yoshihide Ogasawara (Waseda University) for providing the xenolith sample. They thank Raphael Njul, Detlef Krauße, Dorothea Wiesner (BGI), Takeshi Sakai (GRC), Yoshinori Ito, Hiroki Oka, and Hironobu Harada (Tohoku University) for their laboratory support. The authors also thank Catherine A. McCammon (BGI), Horst R. Marschall (Goethe Universität Frankfurt), Michihiko Nakamura (Tohoku University), and Yuto Sato (Kochi JAMSTEC) for the helpful discussion. Constructive reviews by three anonymous reviewers and editorial handling by Jörg Hermann are gratefully acknowledged.

Author contributions

Ryo Fukushima (Conceptualization, Data curation, Funding acquisition, Investigation, Methodology, Project administration, Visualization, Writing—review & editing, Writing—original draft), Tatsuki Tsujimori (Funding acquisition, Resources, Supervision, Writing—review & editing), Nobuyoshi Miyajima (Investigation, Methodology, Supervision, Writing—review & editing), Sayako Inoué (Investigation, Methodology, Writing—review & editing), Tiziana Boffa-Ballaran (Investigation, Methodology, Writing—review & editing), and Giacomo Criniti (Investigation, Methodology, Writing—review & editing)

Downloaded from academic.oup.com/petrology/article/67/10/egag092/8913147 by guest on 30 October 2026

Conflict of interest statement

The authors declare no competing interests.

Funding

This work was supported by BGI at the Universität Bayreuth, and the Joint Usage/Research Center PRIUS, Ehime University, and was funded in part by grants from the JSPS KAKENHI JP22KJ0304, JP25KJ0433 to R.F. (JSPS Research Fellow) and JP21H01174 to T.T. The authors are grateful to the International Joint Graduate Program in Earth and Environmental Sciences, Tohoku University. The Scios FIB and the Titan G2 80-200 S/TEM at BGI were financed by DFG Grant, project number 257745926 and 189856261, respectively.

Data availability

Supplementary figures and tables are available as online supplementary materials. The omphacite CIFs are available on the EarthChem Library (https://doi.org/10.60520/IEDA/114234).

References

Abràmoff, M. D., Magalhães, P. J. & Ram, S. J. (2004). Image processing with ImageJ. *Biophotonics International* **11**, 36–42.

Armstrong, R. L. & Ward, P. (1991). Evolving geographic patterns of Cenozoic magmatism in the North American Cordillera: the temporal and spatial association of magmatism and metamorphic core complexes. *Journal of Geophysical Research: Solid Earth* **96**, 13201–13224. https://doi.org/10.1029/91JB00412.

Atwater, T. (1970). Implications of plate tectonics for the Cenozoic tectonic evolution of western North America. *Geological Society of America Bulletin* **81**, 3513–3536. https://doi.org/10.1130/0016-7606(1970)81[3513:IOPTFT]2.0.CO;2.

Aulbach, S., Pohlner, J. E., Stern, R. A., Höfer, H. E., Schulze, D. J. & Helmstaedt, H. (2026). Sediment-derived deep forearc fluid caused coupled sulfur-Fe^{3+}-enrichment in eclogite from the subducted Farallon plate. *Earth and Planetary Science Letters* **680**, 119883. https://doi.org/10.1016/j.epsl.2026.119883.

Banno, Y., Miyawaki, R., Kogure, T., Matsubara, S., Kamiya, T. & Yamada, S. (2005). Aspidolite, the Na analogue of phlogopite, from Kasugamura, Gifu Prefecture, Central Japan: description and structural data. *Mineralogical Magazine* **69**, 1047–1057. https://doi.org/10.1180/0026461056960307.

Best, M. G., Christiansen, E. H., de Silva, S. & Lipman, P. W. (2016). Slab-rollback ignimbrite flareups in the southern Great Basin and other Cenozoic American arcs: a distinct style of arc volcanism. *Geosphere* **12**, 1097–1135. https://doi.org/10.1130/GES01285.1.

Boffa-Ballaran, T., Carpenter, M. A., Domeneghetti, M. C. & Tazzoli, V. (1998). Structural mechanisms of solid solution and cation ordering in augite-jadeite pyroxenes: I. A macroscopic perspective. *American Mineralogist* **83**, 419–433. https://doi.org/10.2138/am-1998-5-602.

Bunker, B. C. (1994). Molecular mechanisms for corrosion of silica and silicate glasses. *Journal of Non-Crystalline Solids* **179**, 300–308. https://doi.org/10.1016/0022-3093(94)90708-0.

Cámara, F., Nieto, F. & Oberti, R. (1998). Effects of Fe^{2+} and Fe^{3+} contents on cation ordering in omphacite. *European Journal of Mineralogy* **10**, 889–906. https://doi.org/10.1127/ejm/10/5/0889.

van Cappellen, E. & Doukhan, J. C. (1994). Quantitative transmission X-ray microanalysis of ionic compounds. *Ultramicroscopy* **53**, 343–349. https://doi.org/10.1016/0304-3991(94)90047-7.

Carlson, W. D. (2006). Rates of Fe, Mg, Mn, and Ca diffusion in garnet. *American Mineralogist* **91**, 1–11. https://doi.org/10.2138/am.2006.2043.

Carlson, R. W. & Nowell, G. M. (2001). Olivine-poor sources for mantle-derived magmas: Os and Hf isotopic evidence from potassic magmas of the Colorado Plateau. *Geochemistry, Geophysics, Geosystems* **2**, 2000GC000128. https://doi.org/10.1029/2000GC000128.

Carpenter, M. A. (1980). Mechanisms of exsolution in sodic pyroxenes. *Contributions to Mineralogy and Petrology* **71**, 289–300. https://doi.org/10.1007/BF00371671.

Carpenter, M. A. (1982a). Time-temperature-transformation (TTT) analysis of cation disordering in omphacite. *Contributions to Mineralogy and Petrology* **78**, 433–440. https://doi.org/10.1007/BF00375205.

Carpenter, M. A. (1982b). Omphacite microstructures as time-temperature indicators of blueschist-and eclogite-facies metamorphism. *Contributions to Mineralogy and Petrology* **78**, 441–451. https://doi.org/10.1007/BF00375206.

Cesare, B., Acosta-Vigil, A., Bartoli, O. & Ferrero, S. (2015). What can we learn from melt inclusions in migmatites and granulites? *Lithos* **239**, 186–216. https://doi.org//10.1016/j.lithos.2015.09.028.

Chapman, A. D., Rautela, O., Shields, J., Ducea, M. N. & Saleeby, J. (2020). Fate of the lower lithosphere during shallow-angle subduction: the Laramide example. *GSA Today* **30**, 4–10. https://doi.org/10.1130/GSATG412A.1.

Chen, J., Zou, Y. & Chu, X. (2024). DIFFUSUP: a graphical user interface (GUI) software for diffusion modeling. *Applied Computing and Geosciences* **22**, 100157. https://doi.org/10.1016/j.acags.2024.100157.

Cheng, H., Nakamura, E., Kobayashi, K. & Zhou, Z. (2007). Origin of atoll garnets in eclogites and implications for the redistribution of trace elements during slab exhumation in a continental subduction zone. *American Mineralogist* **92**, 1119–1129. https://doi.org/10.2138/am.2007.2343.

Cho, M. & Fawcett, J. J. (1986). A kinetic study of clinochlore and its high temperature equivalent forsterite-cordierite-spinel at 2 kbar water pressure. *American Mineralogist* **71**, 68–77.

Clark, K. F., Foster, C. T. & Damon, P. E. (1982). Cenozoic mineral deposits and subduction-related magmatic arcs in Mexico. *Geological Society of America Bulletin* **93**, 533–544. https://doi.org/10.1130/0016-7606(1982)93<533:CMDASM>2.0.CO;2.

Cliff, G. & Lorimer, G. W. (1975). The quantitative analysis of thin specimens. *Journal of Microscopy* **103**, 203–207. https://doi.org/10.1111/j.1365-2818.1975.tb03895.x.

Coleman, R. G., Lee, D. E., Beatty, L. B. & Brannock, W. W. (1965). Eclogites and eclogites: their differences and similarities. *Geological Society of America Bulletin* **76**, 483–508. https://doi.org/10.1130/0016-7606(1965)76[483:EAETDA]2.0.CO;2.

Condie, K. C. (1982). Plate-tectonics model for Proterozoic continental accretion in the southwestern United States. *Geology* **10**, 37–42. https://doi.org/10.1130/0091-7613(1982)10<37:PMFPCA>2.0.CO;2.

Coney, P. J. (1978) Mesozoic-Cenozoic Cordilleran plate tectonics. In: Smith R. B. & Eaton G. P. (eds) *Cenozoic Tectonics and Regional Geophysics of the Western Cordillera. Geological Society of America Memoir, Vol. 152*, Boulder, Colorado: Geological Society of America, pp.33–50. https://doi.org/10.1130/MEM152-p33.

Coney, P. J. & Reynolds, S. J. (1977). Cordilleran Benioff zones. *Nature* **270**, 403–406. https://doi.org/10.1038/270403a0.

Costa, F., Dungan, M. A. & Singer, B. S. (2001). Magmatic Na-rich phlogopite in a suite of gabbroic crustal xenoliths from Volcán San Pedro, Chilean Andes: evidence for a solvus relation between phlogopite and aspidolite. *American Mineralogist* **86**, 29–35. https://doi.org/10.2138/am-2001-0104.

Downloaded from academic.oup.com/petrology/article/67/10/egag092/8913147 by guest on 30 October 2026

Esperança, S. & Holloway, J. R. (1987). On the origin of some mica-lamprophyres: experimental evidence from a mafic minette. *Contributions to Mineralogy and Petrology* **95**, 207–216. https://doi.org/10.1007/BF00381270.

Faryad, S. W., Klápová, H. & Nosál, L. (2010). Mechanism of formation of atoll garnet during high-pressure metamorphism. *Mineralogical Magazine* **74**, 111–126. https://doi.org/10.1180/minmag.2010.074.1.111.

Feng, P., Wang, L., Brown, M., Johnson, T. E., Kylander-Clark, A. & Piccoli, P. M. (2021). Partial melting of ultrahigh-pressure eclogite by omphacite-breakdown facilitates exhumation of deeply-subducted crust. *Earth and Planetary Science Letters* **554**, 116664. https://doi.org/10.1016/j.epsl.2020.116664.

Ferrero, S. & Angel, R. J. (2018). Micropetrology: are inclusions grains of truth? *Journal of Petrology* **59**, 1671–1700. https://doi.org/10.1093/petrology/egy075.

Ferrero, S., Lorenzon, S., Borriello, R., Borghini, A., Wirth, R., Schreiber, A., Fuchs, R., O'Brien , P. J., Grew, E. S. & Mugnaioli, E. (2026). Pfaffenbergite, $KNa_3(Al_4Si_{12})O_{32}$, a polymorph of sodic feldspar isostructural with kokchetavite and wodegongjieite, found in crystallized melt inclusions in metamorphic garnet. *American Mineralogist* **111**, 60–72. https://doi.org/10.2138/am-2025-9750.

Fleet, M. E., Herzberg, C. T., Bancroft, G. M. & Aldridge, L. P. (1978). Omphacite studies, I. The *P2/n* → *C2/c* transformation. *American Mineralogist* **63**, 1100–1106.

Fukushima, R., Tsujimori, T. & Miyajima, N. (2021). Various antiphase domains in garnet-hosted omphacite in low-temperature eclogite: a FIB-TEM study on heterogeneous ordering processes. *American Mineralogist* **106**, 1596–1605. https://doi.org/10.2138/am-2021-7784.

Fukushima, R., Tsujimori, T. & Miyajima, N. (2024). Simulation of microtextural evolution in omphacite: ordering transformation kinetics as unexplored archives of slab eclogitization. *Physics of the Earth and Planetary Interiors* **354**, 107227. https://doi.org/10.1016/j.pepi.2024.107227.

Giuliani, A., Phillips, D., Kamenetsky, V. S. & Goemann, K. (2016). Constraints on kimberlite ascent mechanisms revealed by phlogopite compositions in kimberlites and mantle xenoliths. *Lithos* **240–243**, 189–201. https://doi.org/10.1016/j.lithos.2015.11.013.

Green, E. C. R., White, R. W., Diener, J. F. A., Powell, R., Holland, T. J. B. & Palin, R. M. (2016). Activity–composition relations for the calculation of partial melting equilibria in metabasic rocks. *Journal of Metamorphic Geology* **34**, 845–869. https://doi.org/10.1111/jmg.12211.

Green, E. C. R., Holland, T. J. B., Powell, R., Weller, O. M. & Riel, N. (2025). Corrigendum to: melting of peridotites through to granites: a simple thermodynamic model in the system KNCFMASHTOCr, and, a thermodynamic model for the subsolidus evolution and melting of peridotite. *Journal of Petrology* **66**, egae079. https://doi.org/10.1093/petrology/egae079.

Hamelin, C., Brady, J. B., Cheney, J. T., Schumacher, J. C., Able, L. M. & Sperry, A. J. (2018). Pseudomorphs after lawsonite from Syros, Greece. *Journal of Petrology* **59**, 2353–2384. https://doi.org/10.1093/petrology/egy099.

Helmstaedt, H. & Doig, R. (1975). Eclogite nodules from kimberlite pipes of the Colorado Plateau—samples of subducted Franciscan-type oceanic lithosphere. *Physics and Chemistry of the Earth* **9**, 95–111.

Helmstaedt, H. & Schulze, D. J. (1988) Eclogite-facies ultramafic xenoliths from Colorado Plateau diatreme breccias: comparison with eclogites in crustal environments, evaluation of the subduction hypothesis, and implications for eclogite xenoliths from diamondiferous kimberlites. In: Smith D. (ed) *Eclogites and Eclogite-Facies Rocks*. Amsterdam: Elsevier, pp.387–450.

Helmstaedt, H., Anderson, O. L. & Gavasci, A. T. (1972). Petrofabric studies of eclogite, spinel-websterite, and spinel-lherzolite xenoliths from kimberlite-bearing breccia pipes in southeastern Utah and northeastern Arizona. *Journal of Geophysical Research* **77**, 4350–4365. https://doi.org/10.1029/JB077i023p04350.

Hernández-Uribe, D. & Palin, R. M. (2019). Catastrophic shear-removal of subcontinental lithospheric mantle beneath the Colorado Plateau by the subducted Farallon slab. *Scientific Reports* **9**, 8153. https://doi.org/10.1038/s41598-019-44628-y.

Holland, T. J. B. & Powell, R. (2011). An improved and extended internally consistent thermodynamic dataset for phases of petrological interest, involving a new equation of state for solids. *Journal of Metamorphic Geology* **29**, 333–383. https://doi.org/10.1111/j.1525-1314.2010.00923.x.

Holland, T. J. B., Green, E. C. R. & Powell, R. (2018). Melting of peridotites through to granites: a simple thermodynamic model in the system KNCFMASHTOCr. *Journal of Petrology* **59**, 881–900. https://doi.org/10.1093/petrology/egy048.

Holland, T. J. B., Green, E. C. R. & Powell, R. (2022). A thermodynamic model for feldspars in $KAlSi_3O_8$–$NaAlSi_3O_8$–$CaAl_2Si_2O_8$ for mineral equilibrium calculations. *Journal of Metamorphic Geology* **40**, 587–600. https://doi.org/10.1111/jmg.12639.

Holness, M. B. & Sawyer, E. W. (2008). On the pseudomorphing of melt-filled pores during the crystallization of migmatites. *Journal of Petrology* **49**, 1343–1363. https://doi.org/10.1093/petrology/egn028.

Hoover, W. F., Page, F. Z., Schulze, D. J., Kitajima, K. & Valley, J. W. (2020). Massive fluid influx beneath the Colorado Plateau (USA) related to slab removal and diatreme emplacement: evidence from oxygen isotope zoning in eclogite xenoliths. *Journal of Petrology* **61**, egaa102. https://doi.org/10.1093/petrology/egaa102.

Hübschle, C. B., Sheldrick, G. M. & Dittrich, B. (2011). ShelXle: a Qt graphical user interface for SHELXL. *Journal of Applied Crystallography* **44**, 1281–1284. https://doi.org/10.1107/S0021889811043202.

Humphreys, E. D. (1995). Post-Laramide removal of the Farallon slab, western United States. *Geology* **23**, 987–990. https://doi.org/10.1130/0091-7613(1995)023<0987:PLROTF>2.3.CO;2.

Humphreys, E., Hessler, E., Dueker, K., Farmer, G. L., Erslev, E. & Atwater, T. (2003). How Laramide-age hydration of North American lithosphere by the Farallon slab controlled subsequent activity in the western United States. *International Geology Review* **45**, 575–595. https://doi.org/10.2747/0020-6814.45.7.575.

Johnson, C. M. (1991). Large-scale crust formation and lithosphere modification beneath middle to late Cenozoic calderas and volcanic fields, western North America. *Journal of Geophysical Research: Solid Earth* **96**, 13485–13507. https://doi.org/10.1029/91JB00304.

Karlstrom, K. E., Wilgus, J., Thacker, J. O., Schmandt, B., Coblentz, D. & Albonico, M. (2022). Tectonics of the Colorado Plateau and its margins. *Annual Review of Earth and Planetary Sciences* **50**, 295–322. https://doi.org/10.1146/annurev-earth-032320-111432.

Kessel, R., Ulmer, P., Pettke, T., Schmidt, M. W. & Thompson, A. B. (2005). The water–basalt system at 4 to 6 GPa: phase relations and second critical endpoint in a K-free eclogite at 700 to 1400 °C. *Earth and Planetary Science Letters* **237**, 873–892. https://doi.org/10.1016/j.epsl.2005.06.018.

Lakey, S. & Hermann, J. (2022). An experimental study of chlorite stability in varied subduction zone lithologies with implications for fluid production, melting, and diapirism in chlorite-rich mélange rocks. *Journal of Petrology* **63**, egac029. https://doi.org/10.1093/petrology/egac029.

Downloaded from academic.oup.com/petrology/article/67/10/egag092/8913147 by guest on 30 October 2026

Lanari, P. & Tedeschi, M. (2025). Chemical map classification in XMapTools. *Applied Computing and Geosciences* **25**, 100230. https://doi.org/10.1016/j.acags.2025.100230.

Lanari, P., Vidal, O., De Andrade, V., Dubacq, B., Lewin, E., Grosch, E. G. & Schwartz, S. (2014). XMapTools: a MATLAB©-based program for electron microprobe X-ray image processing and geothermobarometry. *Computers & Geosciences* **62**, 227–240. https://doi.org/10.1016/j.cageo.2013.08.010.

Lanari, P., Vho, A., Bovay, T., Airaghi, L. & Centrella, S. (2019). Quantitative compositional mapping of mineral phases by electron probe microanalyser. *Geological Society, London, Special Publications* **478**, 39–63. https://doi.org/10.1144/SP478.4.

Lange, T. P., Pálos, Z., Pósfai, M., Berkesi, M., Pekker, P., Szabó, Á., Szabó, C. & Kovács, I. J. (2023). Nanoscale hydrous silicate melt inclusions at the clinopyroxene-amphibole interface in a mantle xenolith from the Perşani Mountains Volcanic Field. *Lithos* **454–455**, 107210. https://doi.org/10.1016/j.lithos.2023.107210.

Laughlin, A. W., Aldrich, M. J., Jr. , Shafiqullah, M. & Husler, J. (1986). Tectonic implications of the age, composition, and orientation of lamprophyre dikes, Navajo volcanic field, Arizona. *Earth and Planetary Science Letters* **76**, 361–374. https://doi.org/10.1016/0012-821X(86)90087-7.

Laurie, A. & Stevens, G. (2012). Water-present eclogite melting to produce Earth's early felsic crust. *Chemical Geology* **314–317**, 83–95. https://doi.org/10.1016/j.chemgeo.2012.05.001.

Leroux , H. , Le Guillou, C., Marinova, M., Laforet, S., Viennet, J. C., Mouloud, B. E., Teurtrie, A., de la Peña, F., Jacob, D., Hallatt, D., Pelaez-Fernandez, M., Troadec, D., Noguchi, T., Matsumoto, T., Miyake, A., Igami, Y., Haruta, M., Saito, H., Hata, S. ... Tsuda, Y. (2024). Phyllosilicates with embedded Fe-based nanophases in Ryugu and Orgueil. *Meteoritics & Planetary Science* **59**, 1947–1965. https://doi.org/10.1111/maps.14101.

Lipman, P. W. (1992) Magmatism in the Cordilleran United States; Progress and problems. In: Burchfiel B. C., Lipman P. W. & Zoback M. L. (eds) *The Geology of North America: Vol. G-3, The Cordilleran Orogen: Conterminous U.S.* Boulder, Colorado: Geological Society of America, pp.481–514. https://doi.org/10.1130/DNAG-GNA-G3.481.

Liu, S., Zhang, G., Zhang, L. & Webb, A. A. G. (2023). Omphacite melting and the destruction of early high-pressure rock records. *Journal of Geophysical Research: Solid Earth* **128**, e2023JB027395. https://doi.org/10.1029/2023JB027395.

Marshall, E. W., Barnes, J. D. & Lassiter, J. C. (2017). The role of serpentinite-derived fluids in metasomatism of the Colorado Plateau (USA) lithospheric mantle. *Geology* **45**, 1103–1106. https://doi.org/10.1130/G39444.1.

Martin, C. & Duchêne, S. (2015). Residual water in hydrous minerals as a kinetic factor for omphacite destabilization into symplectite in the eclogites of Vårdalsneset (WGR, Norway). *Lithos* **232**, 162–173. https://doi.org/10.1016/j.lithos.2015.06.021.

Martin, L. A. J., Ballevre, M., Boulvais, P., Halfpenny, A., Vanderhaeghe, O., Duchêne, S. & Deloule, E. (2011). Garnet re-equilibration by coupled dissolution–reprecipitation: evidence from textural, major element and oxygen isotope zoning of 'cloudy' garnet. *Journal of Metamorphic Geology* **29**, 213–231. https://doi.org/10.1111/j.1525-1314.2010.00912.x.

Masch, L., Wenk, H. R. & Preuss, E. (1985). Electron microscopy study of hyalomylonites—evidence for frictional melting in landslides. *Tectonophysics* **115**, 131–160. https://doi.org/10.1016/0040-1951(85)90103-9.

Matsumoto, T., Tokonami, M. & Morimoto, N. (1975). The crystal structure of omphacite. *American Mineralogist* **60**, 634–641.

McGetchin, T. R. & Silver, L. T. (1970). Compositional relations in minerals from kimberlite and related rocks in the Moses Rock Dike, San Juan County, Utah. *American Mineralogist* **55**, 1738–1771.

McGetchin, T. R. & Silver, L. T. (1972). A crustal-upper-mantle model for the Colorado Plateau based on observations of crystalline rock fragments in the Moses Rock dike. *Journal of Geophysical Research* **77**, 7022–7037. https://doi.org/10.1029/JB077i035p07022.

Morgan, G. B. & London, D. (2005). Effect of current density on the electron microprobe analysis of alkali aluminosilicate glasses. *American Mineralogist* **90**, 1131–1138. https://doi.org/10.2138/am.2005.1769.

Morimoto, N., Fabries, J., Ferguson, A. K., Ginzburg, I. V., Ross, M., Seifert, F. A., Zussman, J., Aoki, K. & Gottardi, G. (1988). Nomenclature of pyroxenes. *Mineralogy and Petrology* **39**, 55–76. https://doi.org/10.1007/BF01226262.

Müller, W. F., Xu, Z. & Brenker, F. E. (2011). Transmission electron microscopy of omphacite and other minerals in eclogites from the CCSD borehole, China: indications for their deformation and temperature history. *European Journal of Mineralogy* **23**, 645–659. https://doi.org/10.1127/0935-1221/2011/0023-2133.

Naeser, C. W. (1971). Geochronology of the Navajo-Hopi diatremes, four corners area. *Journal of Geophysical Research* **76**, 4978–4985. https://doi.org/10.1029/JB076i020p04978.

Nelson, B. W. & Roy, R. (1958). Synthesis of the chlorites and their structural and chemical constitution. *American Mineralogist* **43**, 707–725.

Nishiyama, T. (1989). Kinetics of hydrofracturing and metamorphic veining. *Geology* **17**, 1068–1071. https://doi.org/10.1130/0091-7613(1989)017<1068:KOHAMV>2.3.CO;2.

O'Brien, P. J. (1993). Partially retrograded eclogites of the Münchberg Massif, Germany: records of a multi-stage Variscan uplift history in the Bohemian Massif. *Journal of Metamorphic Geology* **11**, 241–260. https://doi.org/10.1111/j.1525-1314.1993.tb00145.x.

O'Reilly, S. Y. & Griffin, W. L. (2010) Rates of magma ascent: Constraints from mantle-derived xenoliths. In: Dosseto A., Turner S. P. & Van Orman J. A. (eds) *Timescales of Magmatic Processes: From Core to Atmosphere*. London: Blackwell Publishing, pp.116–124. https://doi.org/10.1002/9781444328509.ch6.

Pohlner, J. E., Albert, R., Hao, S., Gerdes, A., Helmstaedt, H. H., Schulze, D. J. & Aulbach, S. (2025). Timing and conditions of UHP metamorphic and metasomatic processes in the subducting Farallon plate revealed by eclogite and omphacitite xenoliths of the Navajo volcanic field (USA). *Contributions to Mineralogy and Petrology* **180**, 27. https://doi.org/10.1007/s00410-025-02218-4.

Pollok, K., Heidelbach, F., John, T. & Langenhorst, F. (2014). Spherulitic omphacite in pseudotachylytes: microstructures related to fast crystal growth from seismic melt at eclogite-facies conditions. *Geochemistry* **74**, 407–418. https://doi.org/10.1016/j.chemer.2014.04.001.

Powell, R., Holland, T. J. B. & Worley, B. (1998). Calculating phase diagrams involving solid solutions via non-linear equations, with examples using THERMOCALC. *Journal of Metamorphic Geology* **16**, 577–588. https://doi.org/10.1111/j.1525-1314.1998.00157.x.

Putnis, A. (2009). Mineral replacement reactions. *Reviews in Mineralogy and Geochemistry* **70**, 87–124. https://doi.org/10.2138/rmg.2009.70.3.

Ralston, S. J., Peretyazhko, T. S., Sutter, B., Ming, D. W., Morris, R. V., Garcia, A. & Ostwald, A. (2023). Phyllosilicate formation on early Mars via open-system acid alteration of basaltic glass. *Earth and Planetary Science Letters* **603**, 117987. https://doi.org/10.1016/j.epsl.2022.117987.

Roden, M. F. (1981). Origin of coexisting minette and ultramafic breccia, Navajo volcanic field. *Contributions to Mineralogy and Petrology* **77**, 195–206. https://doi.org/10.1007/BF00636523.

Roden, M. F., Smith, D. & McDowell, F. W. (1979). Age and extent of potassic volcanism on the Colorado Plateau. *Earth and Planetary*

Downloaded from academic.oup.com/petrology/article/67/10/egag092/8913147 by guest on 30 October 2026

Science Letters **43**, 279–284. https://doi.org/10.1016/0012-821X(79)90212-7.

Russell, J. K. & Jones, T. J. (2023). Transport and eruption of mantle xenoliths creates a lagging problem. *Communications Earth & Environment* **4**, 177. https://doi.org/10.1038/s43247-023-00843-0.

Sakamaki, K., Sato, Y. & Ogasawara, Y. (2016). Hydrous Na-garnet from garnet ridge; products of mantle metasomatism underneath the Colorado Plateau. *Progress in Earth and Planetary Science* **3**, 20. https://doi.org/10.1186/s40645-016-0095-4.

Salviulo, G., Silvestri, A., Molin, G. & Bertoncello, R. (2004). An archaeometric study of the bulk and surface weathering characteristics of early medieval (5th–7th century) glass from the Po valley, northern Italy. *Journal of Archaeological Science* **31**, 295–306. https://doi.org/10.1016/j.jas.2003.08.010.

Schalm, O. & Anaf, W. (2016). Laminated altered layers in historical glass: density variations of silica nanoparticle random packings as explanation for the observed lamellae. *Journal of Non-Crystalline Solids* **442**, 1–16. https://doi.org/10.1016/j.jnoncrysol.2016.03.019.

Schiano, P., Clocchiatti, R., Lorand, J. P., Massare, D., Deloule, E. & Chaussidon, M. (1997). Primitive basaltic melts included in podiform chromites from the Oman ophiolite. *Earth and Planetary Science Letters* **146**, 489–497. https://doi.org/10.1016/S0012-821X(96)00254-3.

Schmandt, B. & Lin, F. C. (2014). P and S wave tomography of the mantle beneath the United States. *Geophysical Research Letters* **41**, 6342–6349. https://doi.org/10.1002/2014GL061231.

Schmidt, M. W. & Poli, S. (1998). Experimentally based water budgets for dehydrating slabs and consequences for arc magma generation. *Earth and Planetary Science Letters* **163**, 361–379. https://doi.org/10.1016/S0012-821X(98)00142-3.

Schmidt, M. W. & Poli, S. (2004). Magmatic epidote. *Reviews in Mineralogy and Geochemistry* **56**, 399–430. https://doi.org/10.2138/gsrmg.56.1.399.

Schulze, D. J., Davis, D. W., Helmstaedt, H. & Joy, B. (2015). Timing of the Cenozoic "great hydration" event beneath the Colorado Plateau: Th-Pb dating of monazite in Navajo volcanic field metamorphic eclogite xenoliths. *Geology* **43**, 727–730. https://doi.org/10.1130/G36932.1.

Segee-Wright, G., Barnes, J. D., Lassiter, J. C., Holmes, D. J., Beaudoin, G. M., Chatterjee, R., Stockli, D. F., Hoffmann, J. E. & John, T. (2023). Halogen enrichment in the North American lithospheric mantle from the dehydration of the Farallon plate. *Geochimica et Cosmochimica Acta* **348**, 187–205. https://doi.org/10.1016/j.gca.2023.03.014.

Segee-Wright, G., Barnes, J. D. & Lassiter, J. C. (2024). Chlorine isotope evidence for Farallon-derived metasomatism of the North American lithospheric mantle. *Geochimica et Cosmochimica Acta* **365**, 70–84. https://doi.org/10.1016/j.gca.2023.11.030.

Seto, Y. & Ohtsuka, M. (2022). ReciPro: free and open-source multipurpose crystallographic software integrating a crystal model database and viewer, diffraction and microscopy simulators, and diffraction data analysis tools. *Applied Crystallography* **55**, 397–410. https://doi.org/10.1107/S1600576722000139.

Sheldrick, G. M. (2015). Crystal structure refinement with SHELXL. *Acta Crystallographica Section C: Structural Chemistry* **71**, 3–8. https://doi.org/10.1107/S2053229614024218.

Smith, D. (1995). Chlorite-rich ultramafic reaction zones in Colorado Plateau xenoliths: recorders of sub-Moho hydration. *Contributions to Mineralogy and Petrology* **121**, 185–200. https://doi.org/10.1007/s004100050098.

Smith, D. (2010). Antigorite peridotite, metaserpentinite, and other inclusions within diatremes on the Colorado Plateau, SW USA: implications for the mantle wedge during low-angle subduction. *Journal of Petrology* **51**, 1355–1379. https://doi.org/10.1093/petrology/egq022.

Smith, D. (2020). Trace elements in Cr-pyrope from the Navajo volcanic field of the Colorado Plateau, SW USA, and implications for the mantle wedge during low-angle subduction. *Lithos* **362–363**, 105460. https://doi.org/10.1016/j.lithos.2020.105460.

Smith, D. & Griffin, W. L. (2005). Garnetite xenoliths and mantle–water interactions below the Colorado Plateau, Southwestern United States. *Journal of Petrology* **46**, 1901–1924. https://doi.org/10.1093/petrology/egi042.

Smith, D. & Levy, S. (1976). Petrology of the Green Knobs diatreme and implications for the upper mantle below the Colorado Plateau. *Earth and Planetary Science Letters* **29**, 107–125. https://doi.org/10.1016/0012-821X(76)90031-5.

Smith, D. & Zientek, M. (1979). Mineral chemistry and zoning in eclogite inclusions from Colorado Plateau diatremes. *Contributions to Mineralogy and Petrology* **69**, 119–131. https://doi.org/10.1007/BF00371855.

Smith, D., Connelly, J. N., Manser, K., Moser, D. E., Housh, T. B., McDowell, F. W. & Mack, L. E. (2004). Evolution of Navajo eclogites and hydration of the mantle wedge below the Colorado Plateau, southwestern United States. *Geochemistry, Geophysics, Geosystems* **5**, Q04005. https://doi.org/10.1029/2003GC000675.

Spear, F. S. (1982). Phase equilibria of amphibolites from the Post Pond Volcanics, Mt. Cube quadrangle, Vermont. *Journal of Petrology* **23**, 383–426. https://doi.org/10.1093/petrology/23.3.383.

Spear, F. S., Hazen, R. M. & Rumble, D. (1981). Wonesite: a new rock-forming silicate from the Post Pond Volcanics, Vermont. *American Mineralogist* **66**, 100–105.

Spera, F. J. (1980) Aspects of magma transport. In: Hargraves E. B. (ed) *Physics of Magmatic Processes*. Princeton University Press: Princeton, pp.265–323.

Tamura, M. (1982). Alteration minerals and mineralization in the Shakanai Kuroko deposit, Akita Prefecture. *Mining Geology* **32**, 379–389. https://doi.org/10.11456/shigenchishitsu1951.32.379.

Tsujimori, T. & Harlow, G. E. (2012). Petrogenetic relationships between jadeitite and associated high-pressure and low-temperature metamorphic rocks in worldwide jadeitite localities: a review. *European Journal of Mineralogy* **24**, 371–390. https://doi.org/10.1127/0935-1221/2012/0024-2193.

Tsujimori, T. & Mattinson, C. (2021) Eclogites in different tectonic settings. In: Elias S. & Alderton D. (eds) *Encyclopedia of Geology*, 2nd edn. London: Academic Press, pp.561–568. https://doi.org/10.1016/B978-0-08-102908-4.00104-1.

Ulmer, P. & Trommsdorff, V. (1995). Serpentine stability to mantle depths and subduction-related magmatism. *Science* **268**, 858–861. https://doi.org/10.1126/science.268.5212.858.

Usui, T., Nakamura, E., Kobayashi, K., Maruyama, S. & Helmstaedt, H. (2003). Fate of the subducted Farallon plate inferred from eclogite xenoliths in the Colorado Plateau. *Geology* **31**, 589–592. https://doi.org/10.1130/0091-7613(2003)031<0589:FOTSFP>2.0.CO;2.

Usui, T., Nakamura, E. & Helmstaedt, H. (2006). Petrology and geochemistry of eclogite xenoliths from the Colorado Plateau: implications for the evolution of subducted oceanic crust. *Journal of Petrology* **47**, 929–964. https://doi.org/10.1093/petrology/egi101.

Usui, T., Kobayashi, K., Nakamura, E. & Helmstaedt, H. (2007). Trace element fractionation in deep subduction zones inferred from a lawsonite-eclogite xenolith from the Colorado Plateau. *Chemical Geology* **239**, 336–351. https://doi.org/10.1016/j.chemgeo.2006.08.009.

Van den Kerkhof, A. M. & Hein, U. F. (2001). Fluid inclusion petrography. *Lithos* **55**, 27–47. https://doi.org/10.1016/S0024-4937(00)00037-2.

Velde, B. (1973). Phase equilibria in the system $MgO–Al_2O_3–SiO_2–H_2O$: chlorites and associated minerals. *Mineralogical Magazine* **39**, 297–312.

Downloaded from academic.oup.com/petrology/article/67/10/egag092/8913147 by guest on 30 October 2026

Warr, L. N. (2021). IMA–CNMNC approved mineral symbols. *Mineralogical Magazine* **85**, 291–320. https://doi.org/10.1180/mgm.2021.43.

Watson, K. D. & Morton, D. M. (1969). Eclogite inclusions in kimberlite pipes at garnet ridge, northeastern Arizona. *American Mineralogist* **54**, 267–285.

Wayte, G. J., Worden, R. H., Rubie, D. C. & Droop, G. T. R. (1989). A TEM study of disequilibrium plagioclase breakdown at high pressure: the role of infiltrating fluid. *Contributions to Mineralogy and Petrology* **101**, 426–437. https://doi.org/10.1007/BF00372216.

Worthington, J. R., Chin, E. J. & Palin, R. M. (2024). Metasomatism of the continental crust and its impact on surface uplift: insights from reactive-transport modelling. *Journal of Metamorphic Geology* **42**, 789–815. https://doi.org/10.1111/jmg.12772.

Yamanaka, T. & Bodine, M. W. (1971). Synthesis of septechlorite solid solution and its equilibrium relation with phlogopite. *Mineralogical Journal* **6**, 383–404. https://doi.org/10.2465/minerj1953.6.383.

Yoder, H. S. (1952). The MgO–Al_2O_3–SiO_2–H_2O system and the related metamorphic facies. *American Journal of Science*, **Bowen Volume**, 569–627.

Zertani, S., Morales, L. F. G. & Menegon, L. (2024). Omphacite breakdown: nucleation and deformation of clinopyroxene-plagioclase symplectites. *Contributions to Mineralogy and Petrology* **179**, 44. https://doi.org/10.1007/s00410-024-02125-0.

Downloaded from academic.oup.com/petrology/article/67/10/egag092/8913147 by guest on 30 October 2026

© The Author(s) 2026. Published by Oxford University Press. All rights reserved. For commercial re-use, please contact reprints@oup.com for reprints and translation rights for reprints. All other permissions can be obtained through our RightsLink service via the Permissions link on the article page on our site—for further information please contact journals.permissions@oup.com.
Journal of Petrology, 2026, 67(10),
https://doi.org/10.1093/petrology/egag092
Original Manuscript

Supplementary figures for:

Melting of lawsonite eclogite xenolith in the Colorado Plateau: Micropetrological constraints on the Oligocene thermal pulse

Ryo Fukushima et al.

This file includes:

Figs. S1–S8

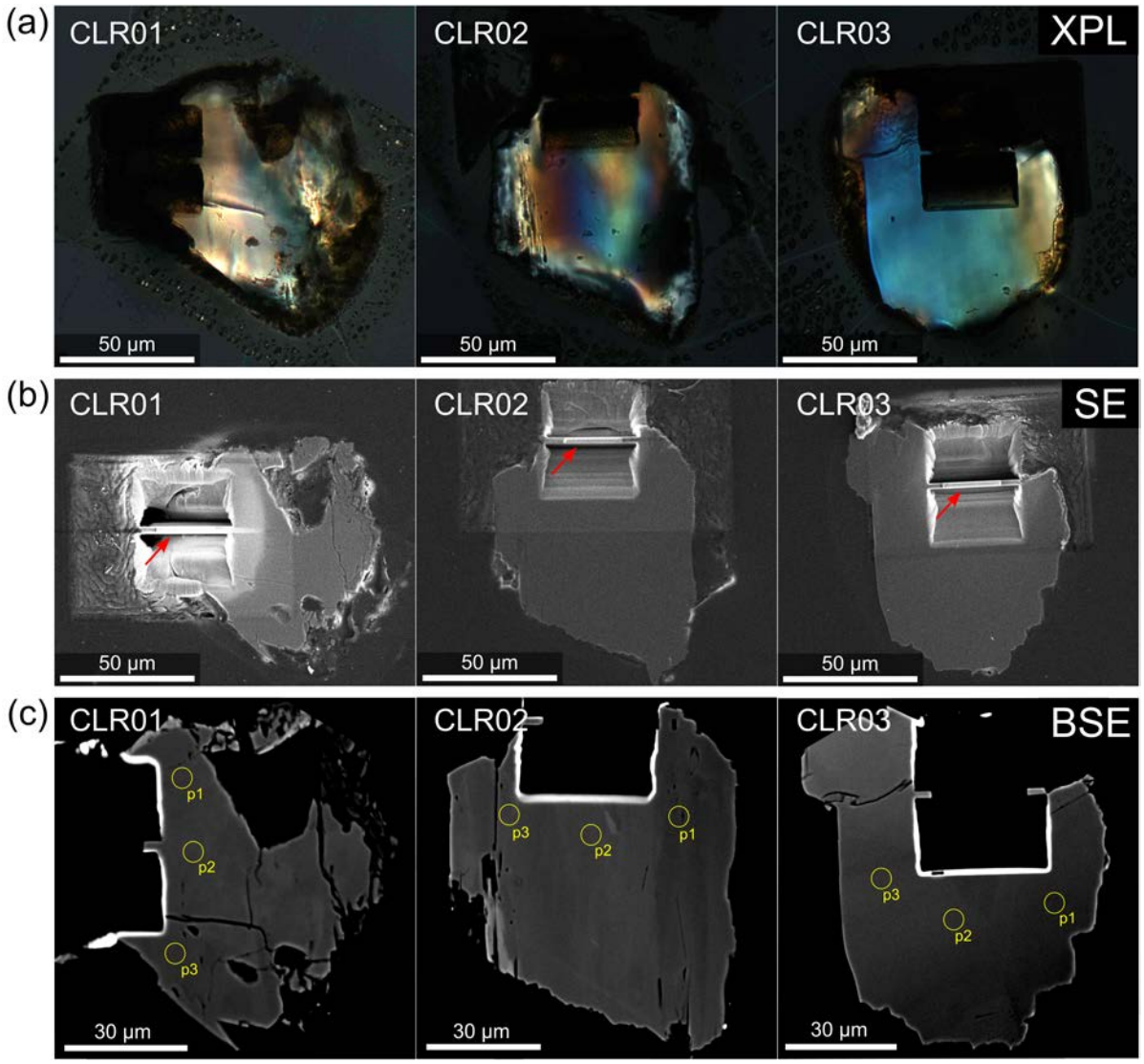


Fig. S1. Microphotographs of the epoxy-mounted omphacite grains (CLR01, CLR02, CLR03). (a) Cross-polarized (XPL) images after the FIB-foil extraction. (b) Secondary electron (SE) images before the FIB-foil extraction, which are indicated by the red arrows (microphotographs taken in the FIB apparatus). (c) Back-scattered electron (BSE) images after the FIB-foil extraction. The regions for the microprobe analyses (indicated by the yellow circles) are approximate, based on rough sketches.

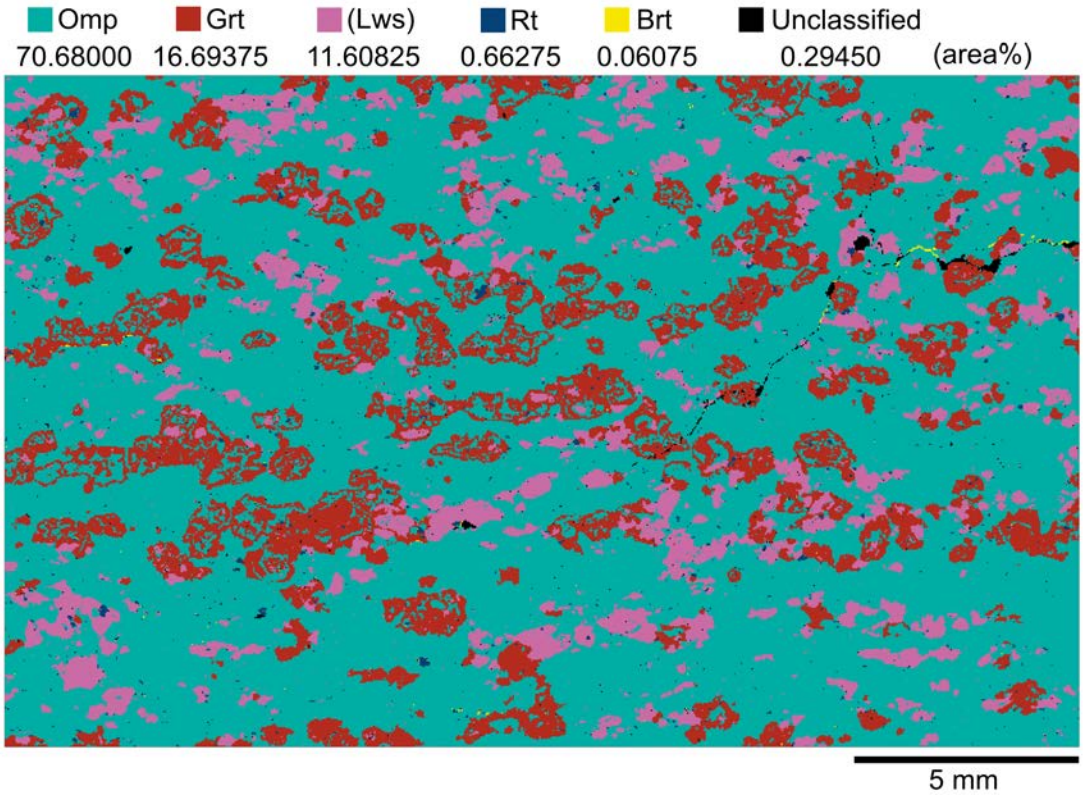


Fig. S2. Thin-section scale phase map of the eclogite xenolith generated from X-ray intensity maps. Measured area proportions of the phases are also presented. Omp = omphacite, Grt = garnet, (Lws) = lawsonite pseudomorphs, Rt = rutile, Brt = barite.

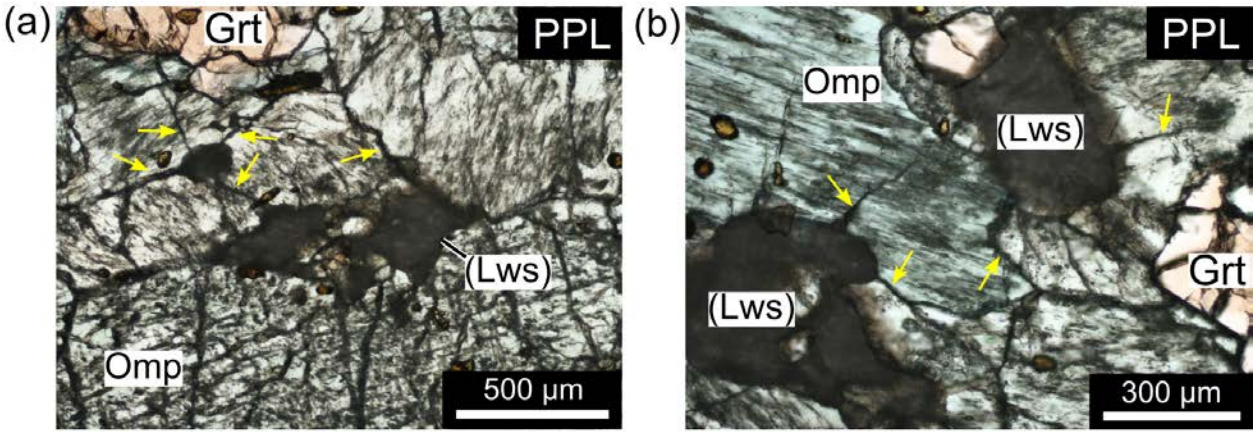


Fig. S3. Plane-polarized (PPL) images of lawsonite pseudomorphs accompanied with radial cracks (indicated by the yellow arrows). (a) An example of radial cracks which appear to extend from lawsonite pseudomorphs. (b) Another example of the similar texture.

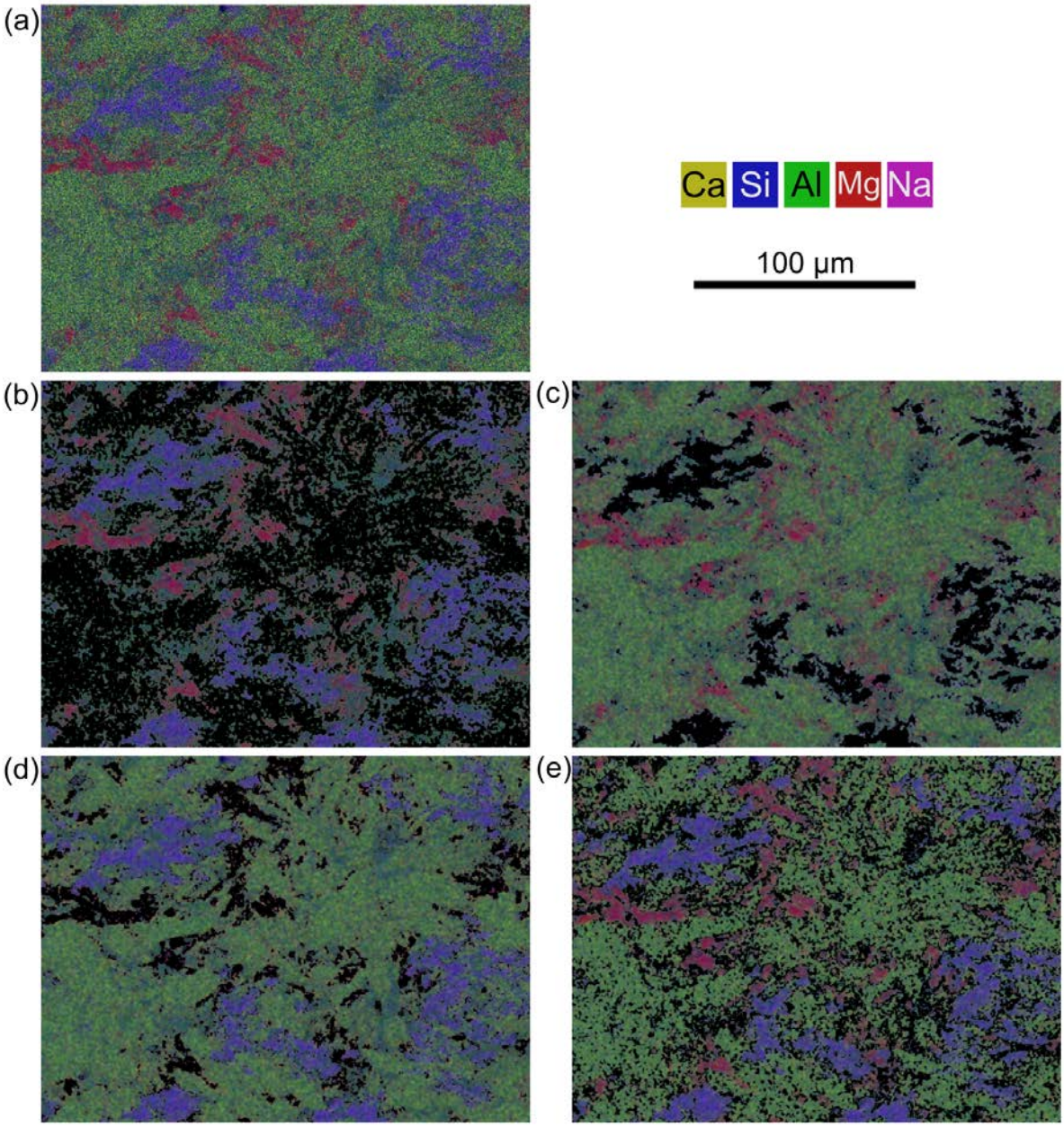


Fig. S4. Processed X-ray maps of the lawsonite pseudomorph. After image smoothing, color thresholding in the L*a*b* color space was applied for calculating the area of each phase. (a) Original X-ray map (same one as presented in Fig. 4a). (b) Mask for zoisite (L* = 96–255, a*,b* = 0–255; area = 10.594). (c) Mask for plagioclase (L* = 0–95, a*= 0–255, b* = 0–111; area = 2.703). (d) Mask for Mg-rich phyllosilicate (L* = 0–95, a*= 129–255, b* = 112–255; area = 2.494). (e) Mask for mica (L* = 0–95, a*= 0–128, b* = 112–255; area = 5.542).

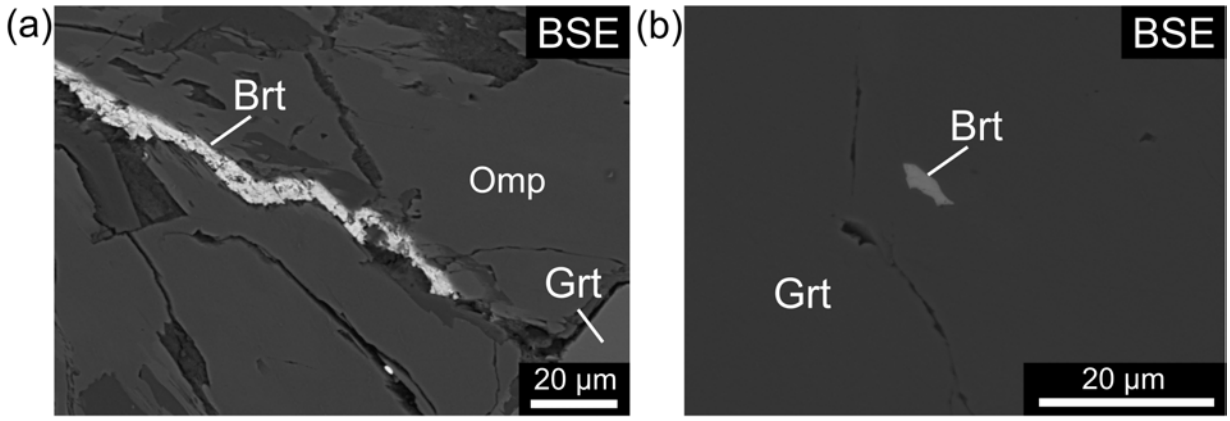


Fig. S5. Occurrence of barite in the xenolith sample. (a) BSE image of a barite vein found in a microcrack in matrix-forming omphacite. (b) BSE image of a barite grain included in garnet.

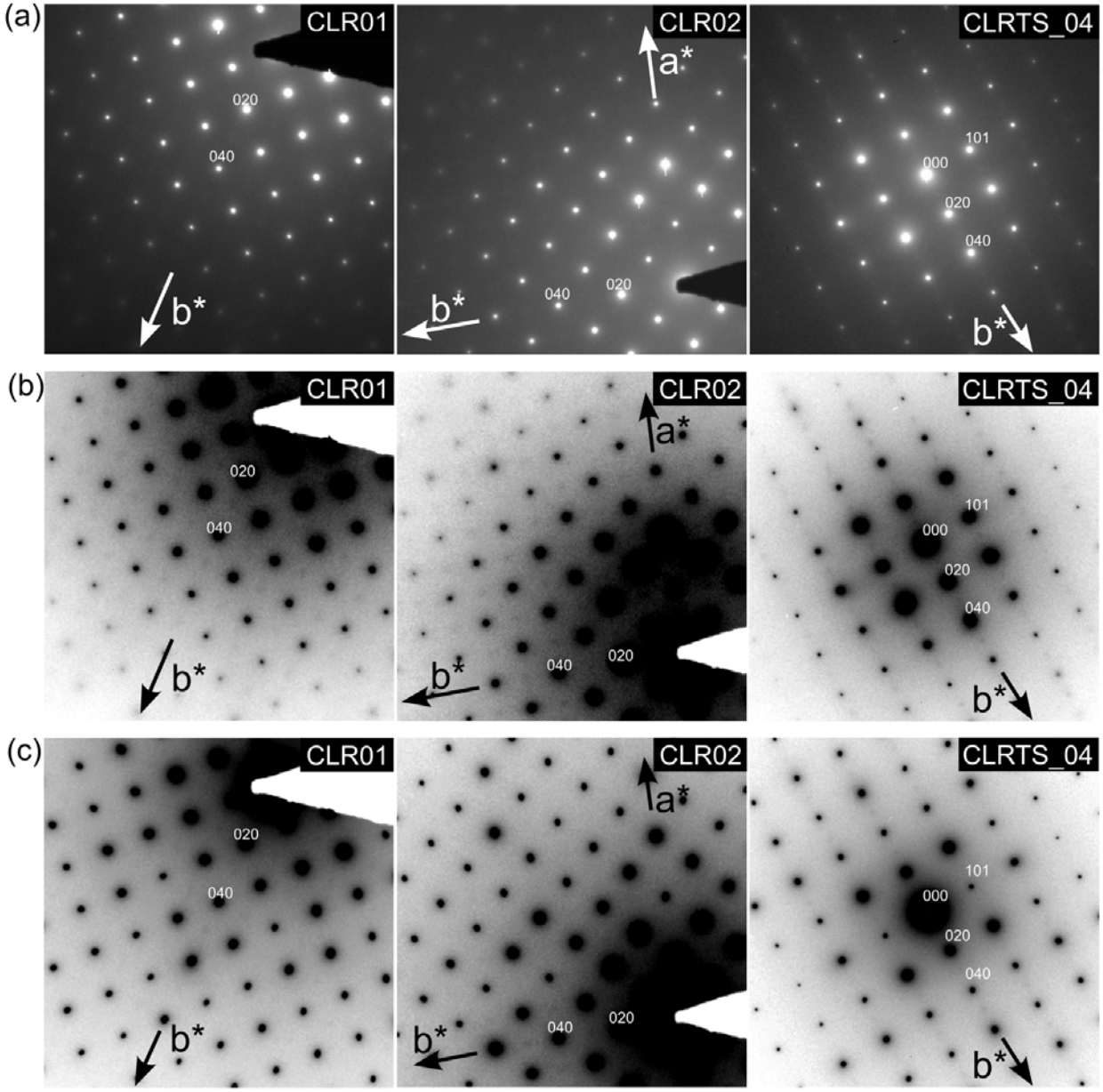


Fig. S6. Selected area electron diffraction (SAED) patterns of omphacite (CLR01 and CLR02: Z = [001]; CLRTS_04: Z = [10$\bar{1}$]). (a) Original SAED patterns. (b) Same images but lightness inversion and brightness-contrast adjustment were applied for emphasizing weak reflections. (c) SAED patterns with a beam precession for the same areas.

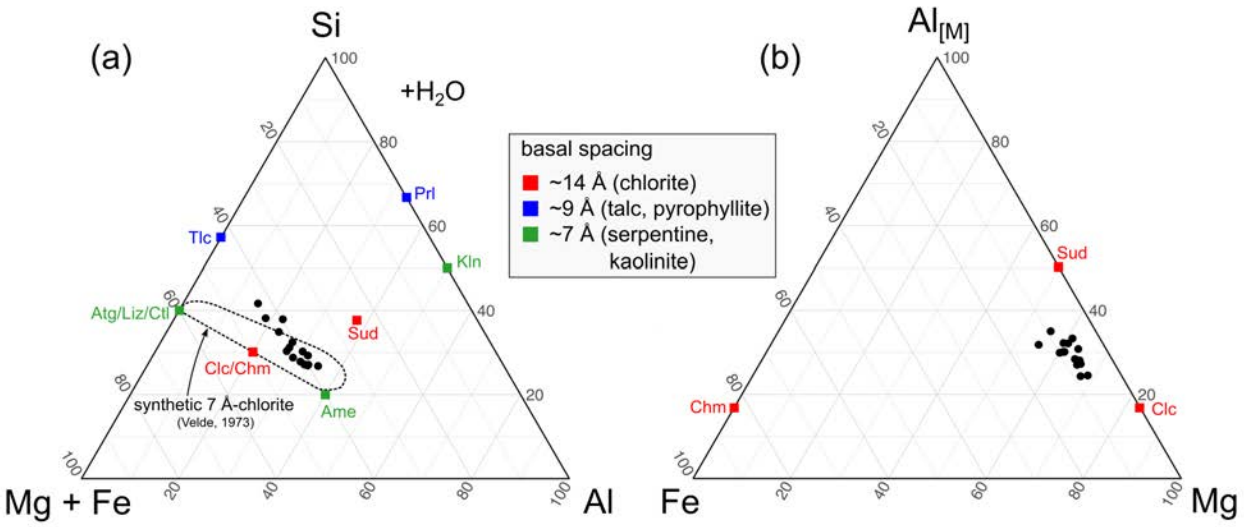


Fig. S7. Compositions of Mg-rich phyllosilicate in lawsonite pseudomorphs. (a) Si–(Mg + Fe)–Al plot. Compositions of several types of phyllosilicate (chlorite, talc, pyrophyllite, serpentine, kaolinite) and the compositional range of synthetic Fe-free 7 Å-chlorite (Velde, 1973) are also presented. (b) $Al_{[M]}$–Fe–Mg plot, where $Al_{[M]} = Al_{total} – (4 – Si)$. Compositions of selected chlorite endmembers (Clc = clinochlore, Chm = chamosite, Sud = sudoite) are also presented.

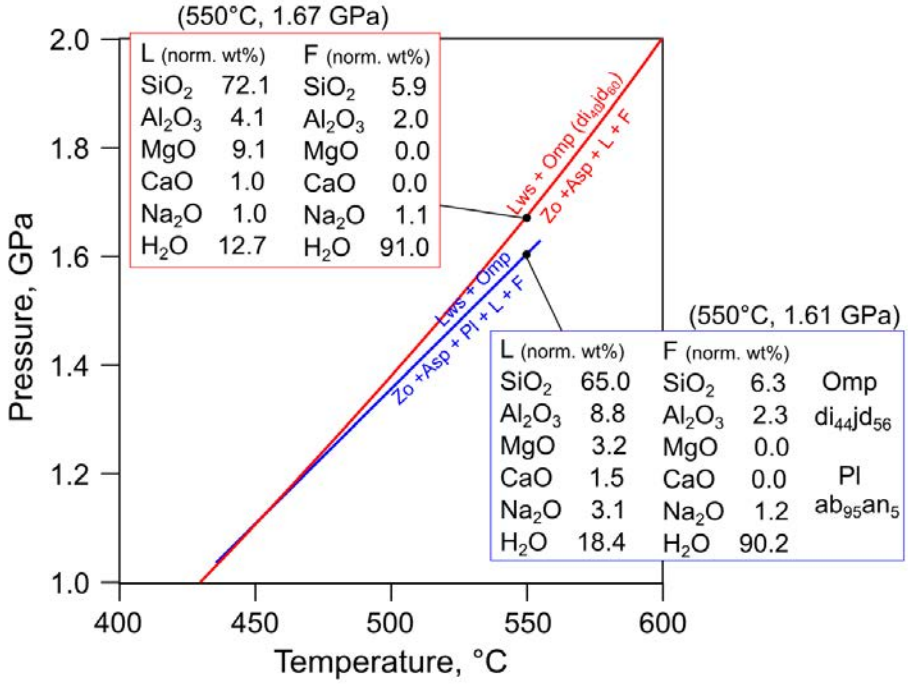


Fig. S8. Aspidolite-forming reactions in the Na_2O–CaO–MgO–Al_2O_3–SiO_2–H_2O (NCMASH) system (red: plagioclase-free, divariant; blue: with plagioclase, univariant). For the plagioclase-free reaction, the omphacite composition was fixed to $di_{40}jd_{60}$ to reduce the degree of freedom. Representative phase compositions are also presented at 550°C. L = hydrous melt, F = solute-bearing aqueous fluid, Zo = zoisite, Asp = aspidolite, Pl = plagioclase.